EUROFUSION WPJET1-PR(14) 12518

JW Coenen et al.

Experimental study of the JET tungsten divertor target melt induced by ELMs: consequences for the plasma facing components and plasma operations

Preprint of Paper to be submitted for publication in Nuclear Fusion

This work has been carried out within the framework of the EUROfusion Consortium and has received funding from the Euratom research and training programme 2014-2018 under grant agreement No 633053. The views and opinions expressed herein do not necessarily reflect those of the European Commission.

ELM-Induced Transient Tungsten Melting in the JET Divertor

J.W. Coenen[2], G. Arnoux[1], B. Bazylev[4], G.F. Matthews[1], A. Autricque[12], I. Balboa[1], M. Clever[2], R. Dejarnac[5], I. Coffey[6], Y. Corre[7], S. Devaux[8], L. Frassinetti[9], E. Gauthier[7], J. Horacek[5], S. Jachmich[3], M. Komm[5], M. Knaup[2], K. Krieger[8], S. Marsen[10], A. Meigs[1], Ph. Mertens[2], R.A. Pitts[11], T. Puetterich[8], M. Rack[2], M. Stamp[1], G. Sergienko[2], P. Tamain[7], V. Thompson[1]
and JET EFDA contributors*

JET-EFDA, Culham Science Centre, OX14 3DB, Abingdon, UK

[1]Culham Centre for Fusion Energy, Abingdon
[2]IEK-4, Forschungszentrum Jülich GmbH, Partner in the Trilateral Euregio Cluster, Juelich, Germany
[3]Laboratory for Plasma Physics, Ecole Royale Militaire/Koninklijke Militaire School
[4]Karlsruhe Institute of Technology, P.O. Box 3640, D-76021 Karlsruhe, Germany
[5]Institute of Plasma Physics AS CR, Za Slovankou 3, 18221 Praha 8, Czech Republic
[6]Astrophysics Research Centre, School of Mathematics and Physics, Queen's Univ. Belfast, UK
[7]CEA, IRFM, F-13108 Saint-Paul-lez-Durance, France
[8]Max-Planck-Institut für Plasmaphysik, 85748 Garching, Germany
[9]Division of Fusion Plasma Physics, KTH, SE-10044 Stockholm, Sweden
[10]Max-Planck-Institut für Plasmaphysik, Teilinsitut Greifswald, D-17491 Greifswald, Germany
[11]ITER Organization, Route de Vinon-sur-Verdon, CS 90 04,613067 St. Paul Lez Durance Cedex, France
[12]Ecole Central Lyon, Lyon, France
** See annex of F. Romanelli et al, "Overview of JET Results", (24th IAEA Fusion Energy Conference, San Diego, USA (2012)).*

Preprint of Paper to be submitted for publication in
Nuclear Fusion

ABSTRACT

The original goals of the JET ITER-like wall included the study of the impact of an all W divertor on plasma operation [1] and fuel retention [2]. As part of the recent decision process by the ITER Organization to begin operations with a full W divertor the focus was put on the issue of transient induced melting and its consequences. JET is the only tokamak able to produce transients / ELMs large enough to allow access to transient melting as potentially can occur at ITER. Transient W melt experiments were performed in JET using a dedicated divertor module and a sequence of $I_P = 3.0MA/B_T = 2.9T$ H-Mode pulses with an input power of P_{IN} =23MW, a stored energy of $\sim 6\,MJ$ and regular type I ELMs at $\Delta W_{ELM} = 0.3$MJ and $f_{ELM} \sim 30$Hz. By moving the outer strike point onto a dedicated leading edge in the W divertor the base temperature was raised within $\sim 1s$ to a level allowing transient ELM-driven melting during the subsequent 0.5s. Such ELMs ($\delta W \sim 300$kJ per ELM) are comparable to mitigated ELMs expected in ITER [3].

Although significant material losses in terms of ejections into the plasma were not observed, there is indirect evidence that some small droplets ($\sim 80\mu m$) were released. Almost $1mm$ ($\sim 6mm^3$) of W was moved by ~ 150 ELMs within 7 subsequent discharges. The impact on the main plasma parameters was minor and no disruptions occurred. The W-melt gradually moved along the leading edge towards the high field side, driven by $j \times B$ forces. The evaporation rate determined from spectroscopy is 100 times less than expected from steady state melting and is thus consistent only with transient melting during the individual ELMs. Analysis of IR data and spectroscopy together with modeling using the MEMOS code [4] point to transient melting as the main process. These experiments provide unique experimental evidence for the absence of significant melt splashing at transient events resembling mitigated ELMs on ITER and establish a key experimental benchmark for the MEMOS code simulations being used to predict transient shallow melting of the ITER W mono-blocks.

BACKGROUND

Until the autumn of 2013 the ITER divertor strategy was to start operation with carbon fibre composite (CFC) tiles at the strike points with W (W) baffles and move to an all-W divertor prior to the nuclear phases in order to minimise tritium retention. This approach was designed to benefit from years of tokamak experience with carbon plasma-facing components (PFC) and to reduce the risks of melt damage in the early (non-active) years of operation when mitigation strategies must be developed against plasma transients (disruptions and Edge Localized Modes (ELMs)). In order both to reduce costs and gain early experience with W, the ITER Organization (IO) proposed in 2011 to eliminate the first CFC-W divertor and begin operations with a full-W variant, to be used until well into the nuclear phase [5]. After a two year period of studies both at the IO and elsewhere the ITER Council (IC) decided in Nov. 2013 to accept the proposal for a full-W start. The results presented here played a major role in this decision process and were in fact attached in preliminary form to the documentation presented to the ITER Science and Technical Advisory Committee prior to the IC decision. This paper provides a more formal and detailed analysis both of the results transmitted to the IO and those presented in earlier papers [6, 7].

1. INTRODUCTION

The use of metallic PFCs (e.g. W) imposes constraints on power-handling due to possible melting $T_{melt}(W) = 3695K$ $(3422°C)$ by uncontrolled thermal loads. The resulting damage may hamper subsequent operation due to reduced thermo-mechanical resilience of the re-solidified surface and can also lead to increased erosion and thus increased radiation cooling of the core plasma by influx of high-Z impurities in the form of vapor and droplets.

Experiments with test-limiters in TEXTOR [8, 9, 10] revealed that melting leads to a strong W source as well as surface modifications Both are subsequently exacerbated by further exposure due to the changed of impact angle on the topologically altered surface, increasing the heat flux there. The effect of geometric modifications, properties of re-solidified material and propagation of melt damage has been well covered by experiments in ASDEX-Upgrade [11, 12, 13], TEXTOR [8] and Alcator C-Mod[11, 14]. Cooling of the main plasma followed by a plasma disruptions is not typical except for events with ejection of large droplets ($> 10\mu m$). Accidental melting of W divertor components in the C-Mod divertor showed that it is not possible to run high performance plasmas on severely damaged W components.

To assess the risk of starting ITER operations with a full W divertor, a key outstanding task was to study the consequences of melting due to rapid plasma transients owing to ELMs and disruptions. Unlike todays devices, ITER plasmas will carry significant stored energy, sufficient to drive W melting at individual events, even on PFCs for which all misaligned edges are protected. In this case, it is important to understand not just the operational impact of melt damaged surfaces, but also understand the relative importance of the different forces acting on the melt layer. Existing laboratory and tokamak melt experiments have shown a range of behavior from plasma pressure driven melt motion [15, 16] causing severe splashing to more benign but deep melt exposures [8].

Of the current operating tokamaks, only JET is large enough to produce transients energetic enough to melt W, and even in this case, the W component must be deliberately engineered to provide an edge on which the power loading can be concentrated, raising the temperature above melting during the transient. This paper describes just such an experiment in which ELM transient heat and particle pulses (~ 300kJ per ELM) are used to load a specially designed misaligned component in the JET divertor in a series of dedicated experimental sessions. An ELM of this magnitude on JET produces an energy density on the divertor target very similar to what is expected for mitigated Type I ELMs on ITER [5, 17, 18]

These dedicated melt experiments were in fact a major research priority for the JET 2013 Scientific Programme [19] in support of the ITER proposal to switch to a full-W divertor for the start of operations. They set out to address the following questions:

- Are the shallow melt-layers produced by transients stable against splashing and how do they move and evolve over multiple events?
- Are the motion and the total amount of molten W in accordance with model predictions and what are the dominant terms in the force balance?

- Do transient events contribute significantly to W contamination of the core plasma and is there any impact on subsequent plasma operations.
- Is the thermal response of an exposed edge as expected, in particular accounting for finite ion Larmor-radius smoothing effects both during and between ELMs?
- Are current codes used in support of ITER reliable for predicting melt-damage and thermal impact on PFCs from given plasma parameters.

Our present capability for predicting the consequences of ELM induced melts in the ITER divertor depends on the answers to these questions. The 3D simulation code MEMOS has been used extensively to predict the behavior and lifetime of ITER and DEMO plasma facing components under various conditions such as runaway electron impact [20, 21, 22, 23, 24, 25, 4, 26, 27, 28], plasma loads during disruptions, ELMs or steady state plasma load conditions.

Key to the success of the JET experiment was to achieve melting of W by transients but avoiding bulk melting which had already been extensively studied in the ASDEX Upgrade and TEXTOR tokamaks [8, 9, 10]. Significant effort has been devoted in the analysis of the experimental results to the question of whether the melt events observed in the JET experiments were induced by ELMs alone or if significant bulk melting was present.

An essential requirement for the design of the experiment was determined by condition that the deliberately misaligned W edge introduced into the JET divertor not compromise normal plasma operation given that once installed, the component would remain in the device throughout the 2013-2014 campaigns. This dictated the choice of location in a single unit of the bulk-W outer divertor (Stack A), Figure 1, which at that time had scarcely been used for other JET experiments.

The paper is structured as follows. Section 2 gives the experimental setup, including a description of the special lamella used and the plasma scenario developed, the key diagnostics used and the data analysis methods. The measurements are described in Section 3 and compared with MEMOS simulations. This section is structured according to the list of questions addressed above: the thermal response of the lamella, the melt dynamics (W production, morphology of the molten/re-solidified material) and the impact on plasma operation are presented. A discussion on whether melting was due to transient or steady state power load is given in Section 3.6. Implications for ITER are discussed in Section 4.

2. EXPERIMENTAL SETUP

2.1. DIVERTOR GEOMETRY AND SPECIAL LAMELLA

The horizontal outer divertor target of JET comprises of 96 tile assemblies (Figure 1) each consisting of 4 stacks of 24 bulk W lamellas (Figure 2 & 1). The top surface of each lamella is shaped [30] in order to shadow the leading edges due to the gaps (typically 1mm) between lamellas. Each lamella is 58mm long (in the radial direction) and typically 5mm wide (in the toroidal direction).

The heat load, q_{div} , onto the divertor targets is a local projection of the parallel heat flux, $q_{||}$, flowing along the magnetic field lines in the scrape-off layer. Due to the low poloidal field in that

region, magnetic field lines strike the targets at a grazing angles to the target surface (typically θ = 1−4°) such that $q_{div} = q_{||} \sin(\theta)$. An exposed leading edge, perpendicular to the target surface is expected from simple geometric considerations to receive a heat load typically 15 to 60 times higher ($\propto 1/tan(\theta)$, $\theta \sim 1$ than on a perfectly aligned surface.

For the purpose of our experiments a specific tile of the horizontal, outer divertor target was modified in order to introduce a leading edge (figure 2) and thereby expose a W surface in JET to transient power densities relevant to the standard divertor (i.e. not misaligned) surface in ITER during an unmitigated transient. This is, however, a compromise since the JET experiment was carried out at normal rather than grazing incidence. This is unavoidable since a full performance ITER pulse will have ~ 60 times the thermal stored energy when compared to the plasmas used for our experiment.

The modification chosen was to lower the eight lamellas in front of the exposed element (magenta lamella in Figure 2). This approach was adopted rather than raising a single lamella to leave open the possibility to study bulk melting including propagation of damage through several lamella. The special lamella and four of the lowered lamellas in front of it have perfectly flat top surfaces rather than the normal compound curve [30]. The exposed surface (figure 2(b)) of the special lamella varies in height from 2.5mm at the inner most side (the high field side (HFS) of the outer divertor) to 0.25mm on the low field side (LFS) side of the lamella. This feature was provided partly to allow variation of the 2D cooling effect as compared to the 1D approximation appropriate to a uniformly heated surface. This cooling effect is strongest for the steady-state heat flux and least effective for transients faster than the timescale for local thermal diffusion. In addition, this geometry provides the possibility of varying the step size with respect the ion gyro-radius and hence study changes to the heat flux distribution for high energetic particle impact during ELMs [31, 32]. The total exposed surface of the leading edge (or the side of the lamella) is: $A_s = 18 \cdot 10^{-6}\text{m}^2$, which is ~ 16 times smaller than the top surface area usually exposed to plasma load: $A_n = 291 \cdot 10^{-6}\text{m}^2$.

The local geometry and frames of reference in the lamella vicinity are illustrated in Figure 3. The geometry is defined using the usual cylindrical machine coordinates: $\{R;\ \phi;\ z\}$ illustrated in black where R is the radial direction, ϕ, the toroidal direction and z the vertical direction. In blue is the local frame of reference of the lamella: $\{x';\ y';\ z'\}$. The magnetic field, $\mathbf{B}$ (illustrated in red), is in the clockwise, or negative toroidal direction (ϕ) viewed from above the divertor. The parallel heat flux, q , is assumed aligned with $\mathbf{B}$. The exposed leading edge is represented in red and the exposed top surface in green. The unit vector normal to the top surface area A_n is defined by the vector $\mathbf{n}$ and to the side surface A_s is defined be the vector $\mathbf{s}$. It is convenient to describe $\mathbf{q}_{||}$ by its two component: $q_n = \mathbf{q}_{||} \cdot \mathbf{n}$ and $q_s = \mathbf{q}_{||} \cdot \mathbf{s}$. Finally, the entire stack is tilted by the angle α_s (figure 3) with respect to the toroidal direction to protect against tile to tile misalignments ($\sin(\alpha_s) = ||\hat{\phi} \times \hat{y}'||$). The standard definition of the geometrical flux enhancement factor is:

$$\eta_q = \frac{q_s}{q_n} = \frac{cos(\theta_\perp + \alpha_s)}{sin(\theta_\perp - \alpha_s)} \tag{1}$$

where the field line angle with respect to the target assuming no tilt ($\alpha s = 0$)

$$\theta_{\perp} = \arctan(B_N / B_{\phi}) \tag{2}$$

B_{ϕ} is the toroidal component of the magnetic field and $B_N = \mathrm{B_p} \cdot \mathrm{N}$ is the projection of the poloidal component of the magnetic field ($\mathbf{B_p} = \mathbf{B_R} + \mathbf{B_z}$) onto the unit normal vector $\mathbf{N}$ ($\sin(\alpha_s) = \mathbf{n} \times \mathbf{N}$). For simplicity, in the rest of this paper the assumption is that $\alpha s = 0$ ($\mathbf{N} \equiv \mathbf{n}$). Figure 4 shows the geometrical flux enhancement factor for the range of $\theta_{\perp}$ experienced on the JET outer divertor target. It also shows that the assumption of $\alpha_s = 0$ overestimates η_q by up to 50% in the worst case at the lowest $\theta_{\perp} = 1.5°$. The actual chamfer angle of Stack A corresponds to $\alpha_s = 0.5°$. This is to be recalled during the thermal analysis of the tile and the comparison with simulations.

2.2. DIAGNOSTICS

In order to quantitatively interpret the outcome of the experiment and also be able to follow the progress of potential melt damage several diagnostics were employed, some installed specifically for the melt exposures.

2.3. IR THERMOGRAPHY

The toroidal installation position of the special lamella was chosen to allow the existing vertically viewing infra-red diagnostics [33, 34] to be used. The so called KL9A and KL9B IR cameras are of the same type ([35]) with KL9A covering the area including the special lamella while KL9B views an unchanged reference part of the outer divertor target toroidally far from the misaligned element (Figure 5(a)).Toroidal symmetry between the two cameras is assumed comparisons. Figure 5(b) shows the actual footprint of the plasma during one of the early exposures of the special lamella, clearly differentiating the temperature rise from its surrounding reference, or flat lamellas.

The vertical viewing geometry means that the IR camera can only see propagation of the heat pulse into the exposed edge of the special lamella from the top. This creates an issue for interpretation particularly for fast events as discussed below. One pixel of the camera is equivalent to $\approx (1.7 \times 1.7) mm^2$ on the top surface of the lamella.

2.3.1. Spectroscopy

The same top window used by the KL9A IR camera was also used for spectroscopic observations focused on a small volume directly surrounding the special lamella. The observation volume of this local spectrometer was determined by backlighting the system with a laser and viewing the resulting spot with JET's in-vessel inspection system (IVIS) – see Figure 6. This showed the viewing spot to have a radius of $3.5cm$ and an overall area of $38cm^2$. Based on the WI 400.88nm line the released amount of tungsten can be estimated as demonstrated in [36, 8]. The emission can then be compared to typical evaporation fluxes at given temperatures [37].

2.3.2. Lamella Imaging

To monitor the progression of the any damage, a high-resolution, vertically viewing, Peltier cooled astronomical camera ([38]) was installed to allow inter-shot images utilizing the IVIS lights, (figure 7(a)). Tests had been carried out in previous JET campaigns to ensure sufficient resilience of the camera to neutron damage and compatibility with the JET environment. The resolution of the system was diffraction limited. One camera pixel corresponds to $57\mu m$ at the target and the limit of resolution is around 2-3 pixels so that objects smaller than about 0.1mm can not be resolved.

The vertical view of the high resolution camera is tangential to the exposed surface of the special lamella and this geometry is optimal for detecting removal of surface material (Figure 7(a)). The actual lamella geometry is shown in photograph of figure 7(b) for comparison also allowing a view on the actual leading edge.

Based on experience in ASDEX-Upgrade, an additional zoomed in video-camera was installed on an existing endoscope system providing a tangential divertor view and opening up the possibility to look for material losses in the form of droplets. This view is limited in resolution to about 1mm, with a frame rate of 20ms, but allows observations of the strike point position and shadowing (see, for example figure 12). This camera was equipped with a $D\alpha$-Line notch filter to allow separation of ELM induced brightness fluctuations from the actual droplets or material emission.

Spectroscopic measurements in the VUV were performed with the aid of a set of survey SPRED spectrometers [39, 40]. Using either routinely a 450g/mm holographic grating in the 10-110nm wavelength range employing a horizontal line-of-sight into the plasma or a spectrometer with a 2105g/mm grating recording spectra in the wavelength range below 40nm and looking nearly vertically down into the JET divertor. This system is sensitive to W ions in the charge state range W_{27+} to W_{35+} which are indicative of the influx of W ions reaching mid-radius of the plasma [41, 42]. Soft X-Ray Data (SXR) ($\sim 0.8nm$) can be used in addition corresponding to emissions closer to the core plasma [41].

2.3.3. Diagnostic Issues

As mentioned above, the KL9A IR camera field of view (FoV) includes the bulk W outer divertor module carrying the special lamella. For this special lamella, measurement of surface temperature is complicated by the geometry of the edge with respect to the camera resolution. Since a single pixel corresponds to 1.7 mm on the object, any strong gradients or sharp edges, such as the corner of the lamella, are not properly resolved. This is not an issue for the reference lamellas since they are sufficiently numerous in the FoV of both IR cameras, the heat flux is toroidally uniform and incident only on the top surface, it is always possible to find a pixel which is representative for the lamella top surface. In contrast, on the special lamella, there is the difficult combination of a steep gradient and an edge

Figure 8(a) illustrates a typical thermal luminance emitted by the special lamella (red). Here simulation is used to illustrate the effect of perfect vs limited resolution. The averaging occurring

by having only pixel per 1.7mm strongly reduces the perceived light intensity (black) leading to an underestimate of the temperature. This effect needs to be corrected for in order to obtain an accurate temperature determination for the edge itself.

The simulation in Figure 8(a) assumes an ideal sensor. Usually, sensor pixels leak to their neighbors and the effective intensity measured by the pixel can be simulated by a Gaussian function with a characteristic width. A value of 17-20% is true for $\sigma = 0$ (Figure 8(a)) but for $\sigma = 0.7$ the real intensity can be underestimated by as much as $\sim 60\%$. A typical value for the pixel characteristic would be $\sigma = 0.5$, which yields an underestimate of the temperature by 40%. Figure 8(b) shows that the derived temperature is quite sensitive to details which are not precisely known. We conclude that uncertainties in the temperature derived from IR will always remain too large due to pixel leakage, system calibration, spatial resolution and emissivity to act as a reliable way of deciding between bulk melting and transient melting in our experiment. Alternative methods are thus required to validate the analysis. Of particular interest is the thermal response of the special lamella on Stack A in comparison to a reference lamella. The method to recover the correct temperature distribution is a 3 step approach (see figure 9).

- We use a flat reference lamella to infer the incident heat flux parallel to the field lines
- The results of step 1 are used to generate a heat load distribution on the special lamella, which is the input for the MEMOS code [4] which subsequently calculates the evolution of the 3D temperature distribution in the special lamella.
- We validate the MEMOS results by generating a synthetic measurement and comparing it with the real measurement.

An example of the measured and synthetic data is shown in figure 10 demonstrating good agreement between model and measurement.This is only possible, however, if certain mitigation factors are applied to the parallel heat flux. Further discussion of this important aspect may be found below in Section 3.4. Additional investigations are given in [7, 43]

2.4. PLASMA SCENARIOS AND CONFIGURATIONS

In order to approach melting cautiously, a plasma scenario was developed in which the outer strike point was swept from stack B (un-modified) to stack A (including the special lamellas) as illustrated in Figure 11. This approach allowed the residence time on Stack A to be selected and hence control the amount of energy deposited on the special lamella. Experimental checks were made to ensure that when the strike line was positioned on Stack A as depicted in Figure 12 (a), no shadowing of the lamella occurred so that the full edge was exposed. Typically the strike line was positioned close to the radial center of the lamella, with an exposure height of $\Delta h \sim 1.3mm$. In order to facilitate understanding of the lamella thermal behavior, additional exposure positions were tested during the experiment preparations. For the melt pulses themselves, the strike line position was maintained away from the exposed edge and only moved towards Stack A for a limited amount of time. By

extending the exposure duration on the special lamella to 1.5s for JET pulse numbers 84778 and beyond, the baseline temperature was increased, allowing the energy delivered by ELMs to drive the special lamella temperature above the melting threshold (figure 13). During the experiments the overall energy deposition limit for the outer horizontal target of 60MJ per Stack has never been reached [44] while the allotment of pulses above $1000°C$ was used for this experiment with pulses reaching ~ $1200°C$ for brief periods even on the normal lamellas.

Although not noticed at the time, erosion of the edge of the lamella was first visible in pulse number 84724 (figure 18) with a hint that small droplets were starting to form at the lower limit of the inter-shot camera resolution of 0.1mm. This is the first indication for melting occurring only during the ELM transients at apparent base temperatures below 2100°C. The temperature history is further discussed in Sec. 3.2 (cf. figure 22). The experiment was performed such that after defining the ideal strike-line position the time duration paired with the ideal base temperature rise was chosen to facilitate transient ELM induced melting. Typical time histories for some key parameters recorded during one of the pulses in which melting occurred are shown in figure 14.

The experiment was performed such that after defining the ideal strike-line position the time duration paired with the ideal base temperature rise was chosen to facilitate transient ELM induced melting.

To generate ELMs with the required energies, the highest possible pedestal pressure was required during the pulses [18]. For this reason a plasma current of $I_P = 3MA$ with a heating power of $P_{IN} = 23MW$ were finally chosen for the melt discharges. These parameters were towards the upper end of what had thus been explored in the JET ILW environment. For pulse numbers 84778 and following the electron pedestal pressure P_e was close to 10kPa (figure 15) leading to maximum ELM loads of $\varepsilon_{||} =\sim 2MJ/m^2$ [18]. The typical ELM size for the exposure conditions was $\Delta_W (ELM) \sim 300kJ$. As seen already from figure 14, no major impact of the melting on the plasma operation can be observed. Only small excursions in P_{rad} hint at ejection of small particles or droplets.

In addition to maximizing the heat flux to the target during ELMs, regular ELMs were required to ensure reproducibility of each melt event. In addition a low frequency was required to allow re-solidification after each ELM.

Figure 16 displays the temperature response of one of the flat reference lamellas during the final adaption of the gas-fueling rate and hence the related changes in ELM temperature rise and frequency. With decreasing fueling-rate, the ELM frequency drops and the apparent temperature rise stabilizes at roughly $200°C$.

From Figure 17 true reproducibility of the pulses in the experiments can be seen with respect to the ELM temperature rise. Even the timing in-between ELMs and within the two compared pulses is almost identical.

3. RESULTS

The most pertinent results come from the experiments in which damage to the special W lamella became visible. In the course of 9 consecutive JET pulses melting was achieved at a plasma current

of 3MA and a combined ion cyclotron resonant heating (ICRH) and neutral beam injection (NBI) power of 23MW. In order to understand the outcome of melt experiments it is important to analyze all measurements and check overall consistency. Available data include the temperature measured on the top surface of the lamella T(x′,y′,t) [°C] from IR thermography and calibrated visible spectroscopy. Spectroscopy allows us to determine the total W release rate W_{eval}[atom/s]. From high resolution imaging we can also determine the surface morphology and compare it with the modeled melt layer motion and amount of material moved. All these quantities must form a coherent picture before we can be sure we understand the observed melt damage.

3.1. MELT DAMAGE AND MATERIAL REDISTRIBUTION

High resolution inter-shot images of the special lamella taken over the sequence of 7 pulses in which melting occurred are shown in figure 18. The first point at which erosion of the lamella edge is visible occurs after pulse number 84724. The next pulse in which plasma was put on the special lamella was pulse number 84778 and here the base temperature was increased. 13. At the same time, the gas fuelling was reduced by 20% to produce more regular ELMs (figure 16). In the subsequent pulse number 84779 the gas fueling was decreased further by 40% yielding almost no difference to the ELM behavior or surface temperature (figure 16). No discharge parameter changes were made in the next 3 pulses. The final pulse of the experiment, pulse number 84785, was an L-mode monitoring pulse run at 2MA and only P_{IN} =2MW with the outer strike point on Stack A, intended to look for signs of any thermally isolated droplets sat on or near the special lamella. The differential images (pulse by pulse Image substraction) in Figure 19 illustrate the subtle differences between the individual pulses and their respective damage. More and More material is moved to the right hand side (HFS) and small droplets occur on the edge of the melt which subsequently move and coalesce. It is also clear that droplets are forming and the position of the material damage is slightly varying. The difference to pulse number 84783 from the previous one is minor as the pulses was ended prematurely and only minor melting occurred.

The observed temperature evolution of pulse number 84778 and subsequent pulses are extremely similar (see Figure 22) so it seems most likely but not certain, that the formation of the large droplet chain at the HFS seen after pulse number 84779 is a cumulative effect rather than the result of a change in the parameters of the incident plasma.

The volume of material moved can be estimated by geometrical arguments. Assuming geometrical shapes e.g. tetrahedrons and prisms one can estimate within a factor of two the volume of material removed from the indented area (Figure 20). This analysis suggests that ~ $6mm^3$ of W were moved during the pulse sequence which is roughly consistent with the estimated volume of the droplets visible on the HFS of the lamella (to be confirmed by post-mortem analysis). There is also clear evidence from these pictures that small droplets move along the edge, coalesce and grow (figure 18).

Careful comparison of the image sequence shows that the large droplet chain at the end of the special lamella gains a new layer of material and grows with each successive pulse in a reproducible

way. At most 1mm of material is removed from the leading edge implying ~ 15 – 300μm per melt exposure and hence close to 10μm per ELM.

3.2. THERMAL RESPONSE

An essential ingredient in our attempts to model the W melt layers has been to ensure that the thermal model used in the MEMOS code provides a surface temperature distribution and time history consistent with the experiment (cf section 2.3.3). Data from the flat reference lamella has been used to evaluate the thermal response of conventional surfaces with respect to heat flux impact and temperature behavior. Figure 21 shows a comparison of typical IR temperature data around the time of an ELM from a flat reference lamella with the image of the damage, indicating a direct relationship between the two. One can see that the maximum temperature between ELMs is centered further in that the damage pattern which provides the first evidence that the primary cause of the melt damage was the ELMs.

Figure 22 displays the as-measured peak temperature values on both a flat reference as well as the special lamella for each of the four 1.5s long melt exposure pulses where most of the change was observed (pulse numbers 84778–82).

The reproducibility of the temperature evolution between the different pulses is apparent as well as the differences between the special and the flat reference lamellas. The measured (uncorrected) temperature rise for the special lamella is $\Delta T \sim 2100°C$ with the peak close to $2300°C$ while the flat reference lamella at most heats up to $1100°C$. As already discussed, due to the limited resolution of the IR diagnostics, the temperature of the leading edge of the special lamella is underestimated. On slow timescales, the effect can be up to 30% while during ELMs a factor of 3-5 is predicted by thermal modeling combined with simulation of the diagnostic response (Sec. 2.3.3, [7, 43]). This means that the inter-ELM temperature of the special lamella is much closer to $2800°C$ with an additional ELM induced temperature rise of ~ $1000°C$. On this basis we conclude that melting during each ELM can be achieved (Section 2.3.3).

If we compare the temperature ratio between the flat reference lamella and special lamella in figure 22 it is apparent that even with the diagnostic temperature corrections, the ratio is well short of the factor 25 we might expect from the simple geometric arguments presented earlier in figure 4. Even though the direct relation between ΔT and Δ_q is only observed assuming 1D heat diffusion, we will next show that taking into account full 3D modeling does not resolve the issue relating to the missing heat flux. Put another way, simple geometric projection of the heat fluxes from the flat reference lamellas to the leading edge of the special lamella produces model results which are inconsistent with corrected IR data, evaporation rate, Planck radiation and melt dynamics.

3.3. THERMAL MODELLING AND MELT-LAYER DYNAMICS

We have employed 3D modeling with the MEMOS code to test the consistency of the surface power flux densities determined from IR observation of flat reference lamellas, spectroscopic

measurements and melt layer imaging of the special lamella. Figure 23 illustrates the geometric assumptions employed here. For the heat flux impinging on the top surfaces (q_n) only a moderate gradient is present along the lamella (x′) in addition to a negligible gradient in the toroidal direction (y′). For the heat flux impinging on the side surfaces however a very in-homogenous loading is present. Our starting point in the modeling was to use the measured perpendicular heat-flux on a flat reference lamella as input to the MEMOS 3D thermal model and melt layer dynamic code which has been extensively used in support of ITER. The MEMOS simulations and the measurements are compared in Figure 24 for pulse number 84779. T_{MEMOS} (in black in Figure 24 (b)) suggests that bulk melting of the special lamella should have occurred around t = 13.2s. For this simulation, the corresponding W vaporization flux W_{vap} is ~ 100 times higher than that measured (Figure 24 (c)).

The evaporation source from the exposed edge can be spectroscopically determined. The emission can then be compared to typically evaporation fluxes at given temperatures [37]. The much higher vaporization rate translates to a depth of melted material of about 450μm per pulse ~ 2 times higher than estimated from observations with the high resolution camera. This suggests that the $q_s(x', t)$ used as input to the MEMOS simulations is far too high.

The MEMOS output includes a full time history of the predicted W evaporation rate and this has been averaged over the integration time of the spectrometer (100ms). This analysis shows that the observed evaporation rate is dominated by ELMs. In Figure 25 the measured (figure 25(a)) values during the exposure are compared with the calculated values (figure 25(b)). One can see that the peak evaporated flux is $\sim 6 \cdot 10^{19} m^{-2} s^{-1}$ is much below the theoretical value for a situation close to the melting point of W (figure 25(b)). Only by taking into account the limited temporal resolution of the spectrometer can we account for this discrepancy. Within each typical frame taken by the spectrometer (100ms) there are 3 ELMs each of 3 ms duration meaning that the observation is consistent with a maximum evaporation flux of $\sim 10^{22} m^{-2} s^{-1}$ during each ELM.

In order to match the experimentally observed situation a mitigation factor with $0 < f_{n,s} < 1$ is applied to the heat flux reaching the top and side surfaces of the lamella. From eq. 1,2:

$$q_{s,ref} = q_{perp} / tan(\theta_{perp}) \tag{3}$$

$$q_n = f_n * q_{n,ref} = f_s * q_{perp} \tag{4}$$

$$q_s = f_s * q_{s,ref} \tag{5}$$

The mitigation factor is applied to the parallel heat flux reaching the exposed edge and is close to $f_s = 0.4$. q_n can be directly measured and is used as the input quantity f_n remains unity. For both H-Mode and L-Mode conditions a mitigation factor is required for consistent MEMOS modeling of the special lamella temperature but MEMOS accurately predicts the temperature of a flat reference lamella using the uncorrected heat flux derived from standard IR analysis [7]. Several iterations were required to converge on the best case for witch $f_s = 0.4$ is found.

So far, a clear physics understanding of the mitigating factor is lacking.Some possibilities are discussed below (Section 3.4). With further understanding improving as part of the ongoing analysis

factors dependent on exposure conditions may prove necessary potentially seperating for ELM and inter-ELM phases. In the case of $f_s = 0.4$ Figure 24 (d) shows a fair agreement of W_{vap} between the simulation and measurement, with a melt depth of 200μm consistent with the estimates from the quantity of displaced material (Figure 20).

The temperature profiles show a very good agreement, at least in the SOL ($x' > 20$ mm - black and blue curves) for both the inter-ELM (Figure 24 (e)) and ELM (Figure 24 (f)) phases. The good agreement of 3 independent observations (Evaporisation Flux, Surface Damage, IR Temperature) and the fact that the simulated temperatures are in fair agreement with the measurement strongly suggests that the melting was induced by transients only, since the inter ELM temperature simulated (red curve in Figure 24 (b) does not cross the melt threshold. Note that the disagreement between the simulated temperature and the measurement in the private flux region is due to the constraint we placed on the fitted inter-ELM profiles. This forced the private region profile seen with with KL9A to be consistent with that seen with KL9B [7]. Analysis is ongoing to check for a potential toroidal asymmetry. In order to obtain the correct temperature distribution and melt layer motion consistent between observation and simulation, we might need to use a different heat flux reduction factor during and between ELMs: $f_{s,ELM}$ and $f_{s,inter-ELM}$. We also note that W_{vap} in the simulation is higher a the beginning of the pulse and is in better agreement near the end. This suggest that f_s is probably not constant in time. These complicating factors make it difficult to achieve a fully consistent picture without a direct temperature measurement on the exposed side face of the special lamella.

The question is then why do we need f_s? Is it real, or an artifact of the measurements? The latter can be ruled out. One could argue that q_s is too high because q_n is overestimated. We have verified that q_n is consistent with measurements in other experiments (e.g. $\varepsilon_{peak,elm}$ scales with P_{ped} as in [18]) and that a reasonable energy balance between input power and deposited power is achieved. The causes of this missing heat load are a matter for future investigation but it is potentially a positive result for ITER since leading edges might not be as vulnerable as one might think. However, further work is need to understand the physics reason for this missing heat flux since the specific geometry used in JET may play an important role (misalignments on the scale of 1mm will not occur in the high heat flux regions of the ITER divertor).

After applying the ad-hoc heat flux mitigation factor and having reproduced the observed temperature evolution and spectroscopic data with the modeling we can now use MEMOS to estimate the actual melt damage and redistribution ([20])

Figure 26 shows the calculated melt layer redistribution assuming a $f_s = 0.4$ as also used in figure 24. A single exposure pulse is modeled based on the heat flux data given for pulse number 84779 (cf. Figure 24). The MEMOS modeling of this pulse finds that the ELM-induced melt layer moves towards the HFS with one pulse moving ~ 200μm originating to a thermo electric current hence a j × B force as seen in previous melt experiments [24].

3.4. MITIGATION FACTORS

One obvious candidate to explain the necessary ad-hoc heat flux mitigation factor is the so called finite ion gryo-radius smoothing effect. This can smooth the power load on the edge [32] if the height of the exposed edge, h, is comparable to ρL (Ion-Larmor-radius). During ELMs one finds $\rho_L \sim h$, but not during the inter-ELM phases where $\rho_L << h$. PIC (particle-in-cell) simulations for this JET experiment have demonstrated that this would reduce the heat load by at most 25% during ELMs [31]. Even if there is thus a small contribution during the ELMs, this cannot be an explanation for the need of a mitigation factor for the heat flux between ELMs. Inter-ELM phases are most likely similar to L-Mode condition. Note that $fs \simeq 0.2$ is necessary even in L-mode plasmas, where the lamella temperature is far from melting conditions and $\rho L << h$.

Extensive analysis of this possibility has been carried out using the same particle-in-cell code (PIC) that had previously been used to predict such effects in ITER and JET [31, 32, 45]. The key physics parameter for this process is the ratio between the step size and the ion gyro-radius. For this reason the effect would be expected to be largest during an ELM event when the local temperature is thought to be comparable to the pedestal temperature.

Figure 27 displays simulation results for the heat flux at the corner of the misaligned tile normalized to the available parallel heat flux $q_{||}$ as a function of the step size normalized to the ion gyro-radius and for 3 distinct assumptions on ELM pedestal characteristics. Points represent a leading edge of 1.5mm which is close to the experimental value."

By applying pedestal and geometric factors relevant to the ELMs seen in the experiment (Table 1) and using a simple thermal model, this work has concluded that redistribution of the heat flux along the leading edge but might account for only 20% of the observed effect.

Not only is the predicted effect too small to explain what we have observed but it is also visible during L-Mode as well as H-Mode. This provides the strongest evidence that ion Larmor radius effects are not the dominant cause because we would expect them to be much weaker between ELMs and in L-mode plasmas.

Without an understanding of the physics behind the mitigation of the heat load the edge of special lamella it is hard to make predictions but the result appears rather positive in that it reduces the extent to which accidentally exposed edges will limit divertor power handling.

3.4.1. Alternative Mitigation Physics

From exposures during L-Mode one can deduce that also here a mitigation factor of 0.2 is required i.e. half that used in the H-mode melt experiments. This leads to the possibility that ELM and Inter-ELM mitigation factors are different. Simulations based on this idea hint at higher f_s during the ELM and lower f_s in-between which if true might suggest that the effect might be connected to local recycling or energy reflection. However, q_{perp} from the IR measurement is the effective transmission of heat flux to the surface - already including energy and particle reflection and local recycling so these factors can only offer an explanation if they are strongly enhanced for normal incidence of

the heat flux. In [46] it was suggested that the relatively high momentum and energy reflection for deuterium on W might mitigate the incoming heat flux. For the shallow angle exposure of the flat reference lamella this effect could be much weaker since the reflected particles are not directed back against the incoming flow. At this stage such ideas are purely speculative and quantitative modeling is required to demonstrate plausibility. Effects like local recycling may also play a role in mitigating transients [47].

Finally, one could speculate that the specific geometry of the modified stack generates local turbulence that enhances the perpendicular transport locally and redistributes the heat flux to neighboring lamellas in what should be the shadowed area. However, analysis of the energy arriving at lamellas in front of the special lamella where any deflected heat flux might be expected to be deposited has so far not revealed any significant anomaly with respect to the expected geometric factors.

Figure figure 28 shows the calculated and measured shadow line and hence the power deposited. Analysis of the heat-lux to neighboring lamellas does so far not find excess deposition.

3.5. PLASMA IMPACT

In considering the possible impact of the JET melt experiment on tokamak operation two main aspects need to be taken into account. The first is the W source originating from evaporation of the strongly heated and molten exposed surface and the second is the potential for molten W droplets or solid particles to be expelled into the plasma. The impact of these sources on the core plasma depends on the screening factors that apply in each case as well as the core impurity transport properties for high Z elements.

No enhanced W influx above the observed background variation was visible in W VUV spectra recorded in the main plasma for any of the pulses run on Stack A prior to those in which melting was observed.

Figure29 shows data from the main chamber VUV spectrometer,together with the time variation of the outer divertor strike point location. In pulse number 84724, despite the excursion to Stack A, no W expulsion was seen and only minor melting was visible in the post exposure inspection (figure 18). Figure 29 shows an enhanced W level when the strike point is positioned on Stack A. This increase can be attributed to enhanced erosion of the leading edge. Strong evaporation is only present for the actual melt exposures showing transient melting (cf. Figure 25).

During pulse number 84778 and the following pulses, clear evidence of W expulsion in the form of spikes is apparent from the VUV signals during the time spent on Stack A. There is no enhanced W signal before and after this period. As pointed earlier, the main difference between pulse number 84724 and subsequent melt exposures is the time the strike point resides on Stack A. The later pulses have 0.5s longer exposure and thus higherbase temperature on the special lamella, allowing each ELM to go further above the melt threshold. The VUV signals suggest that motion of the molten material leads to expulsion of small droplets.

Looking at the evolution between pulses, the following observations can be made: For pulse number 84778 droplet expulsion occurs late and with increasing intensity, while for pulse number 84779 a droplet is already expelled early on when the strike point is on Stack A. For the pulse numbers 84781–83 droplet activity decreases, with only one large event in pulse number 84783. This could be interpreted as a conditioning effect of the surface. The largest melt progression occurs during pulse number 84779. This pulse had the minimum gas fueling, 30% lower than the preceding pulse though the inter-ELM temperature is not increased compared to the previous pulse, see Figure 16. Pulse number 84783 was terminated early by the plasma control system due to excess radiation after the W event disturbed the plasma, no disruption occurred.

Careful study of the video record failed to identify signs of droplet expulsion in any of the divertor camera views. One can however determine the timing of the droplet release and the movement of the respective material by indirect spectroscopic means. Figure 30 shows for two of the melt pulses time traces from the divertor W spectroscopy diagnostic (figure 6), together with the mid radius VUV W emissions ($\sim 5nm$) and soft X-ray data corresponding to the core plasma [41].

From this combination of data a clear chain of events can be deduced. The droplets are emitted locally but do not fully ablate in the divertor region.The Tungsten atoms then reach the edge of the main plasma and later the core. From a calibration of the SXR diagnostic a rough estimate of the quality of W entering the main plasma can be determined. This analysis suggests that close to $5 \times 10^{16} - 10^{17}$ atoms reach the main plasma - corresponding to the content of a W sphere with a radius of $80–100\mu m$. An important question is whether such a W droplet can survive long enough to reach the core. Information relevant to this question can be found in [13, 12, 8]. The typical $q_{||,\, inter–ELM}$) for these conditions is $\sim 500 MW/m^2$ which leaves droplets a sufficient lifetime to move a significant distance through the plasma as seen from figure 31.

The validity of the droplet analysis in our experiment has been demonstrated using a W Laser Blow Off experiment (LBO) from a main chamber position which was performed in a similar plasma at 3MW/23 MW. Figure 32 compares a single melt droplet event melt event with a LBO pulse under approximately the same plasma conditions.

With a similar amount of W expelled from the LBO to the one expect in the melt droplets the impact on the plasma is very similar, suggesting penetration to the main plasma. This indicates that at least some droplets are not strongly screened which is consistent with modeling. We will not know how many droplets might not have made it to the main plasma until the special lamella is removed from JET and accurately weighed to determine the mass loss. This is currently expected for early 2015.

3.6. TRANSIENT VS. BULK MELTING – DISCUSSION

One of the main issues arising during the interpretation of this experiment requires further elaboration: bulk versus transient melting. From the material presented thus far we can draw the following conclusions:

- The modeled IR response is consistent with a base temperature of the special lamella below the melting point.
- The total melt depth of ~ 1*mm* (150–300μm per shot) implied from the pulse-to-pulse high resolution photography requires transient melting to be the dominant mechanism; steady state melting would lead to melting of ~ 2*mm* per pulse.
- The W evaporation rate is consistent only with transient melting.
- Allowing for a mitigated heat-flux (due to an as yet not understood cause), MEMOS can match not only the observed temperature evolution, the actual melt depth and W redistribution pattern, but also the evaporation rate and Planck radiation (quantities determined independently by experimental observation).
- The first sign of erosion was seen already during pulse number 87724 which had a 0.5s shorter phase on Stack A and so significantly lower inter-ELM temperature at the end of the pulse still allowing transient melting by ELMs.
- The peak in the observed erosion is most consistent with the location where the ELMs strike the lamella and not with the position of the maximum inter-ELM heat flux which is further inwards (towards the HFS).

For an example of steady state deep melting refer to [11]

4. IMPLICATIONS FOR ITER

There was intense interest in the outcome of the JET experiments because a decision on whether to start ITER operations with a full W divertor was to be taken in October 2013. The JET experiment was aimed primarily at answering the question as to what might happen in the event of transient surface melting on the ITER W divertor due to unmitigated Type I ELMs, the mitigation of which cannot be completely guaranteed for all events in ITER. A key benefit of trying to answer this question is the experimental data which this generates for validation of the MEMOS melt code, the primary tool being used for simulations on ITER to assess that the risks of starting with a full-W divertor are acceptable. An apparently positive result in JET might not necessarily scale favorably to ITER and so caution is required in interpreting the results in a direct way.

4.1. REMAINING UNCERTAINTIES:

- While the JET experiment shows that there is no immediate consequence of ELM-induced erosion of a single exposed edge, ITER has the potential to produce similar damage over the whole surface area of the divertor in the strike point regions of the strike point. The number of droplets produced could therefore be much larger. Whether or not this would be sufficient to disrupt an ITER plasma cannot be simply concluded from the JET experiment, but the results do provide the basis for such an analysis. Such calculations are not within the scope of this paper.
- Although relatively few droplets were ejected in the JET experiments and appear to have been very

small, the results do show there is a process by which small droplets migrate, coalesce and grow which will always be difficult to capture in a code such as MEMOS. This means that continued operation above the damage threshold may accumulate droplets of sufficient size that they could pose a significant disruption risk if ejected into the ITER plasma. Once again ITER specific calculations would be required to determine how large and how many such droplets would pose a threat since the screening in ITER is expected to be significantly higher than in JET.

- Given the relatively short time spent over the melting threshold in the JET experiments one can see that the erosion rate is high and this could be an issue in ITER even if there were no other consequences. This supports the need for early detection in ITER coupled with mitigation measures to avoid large scale melting of divertor surfaces.

4.2. POSITIVE FINDINGS FOR ITER:

Despite the remaining uncertainties listed above, a number of findings point to this JET experiment having a favorable outcome for the decision to begin operations on ITER with a full-W divertor:

- Although scaling of ELM energy densities to ITER was not the aim of this particular experiment, the fact that JET needed to operate at relatively high input power and current to preheat an edge at normal incidence to the ELM heat flux shows that it is not so easy to induce melting by ELMs. To illustrate this point, one can see that to achieve melting from a starting temperature of around $1000°C$ on the normal W lamellas in JET with all other things being equal we would have to increase the plasma thermal stored energy from 6 to about 60MJ. This is a similar stored energy to that expected in the low activation phase of ITER. ITER however has twice the major radius and twice the divertor flux expansion as that used in these JET experiments, so there is roughly a factor four margin. These numbers appear roughly consistent with the estimations in [5] for ELMs with a factor of four broadening and support the idea that there a low risk of transient melting by ELMs in the early phases of ITER operation (unless divertor mono-block edges are exposed).Such conclusions do not, of course, apply to the nuclear phases of operation, where stored energies in ITER should be at the several 100MJ level.
- JET ran a series of 7 very reproducible 3 MA discharges with 23 MW of heating without a single disruption despite progressive melting of a grossly misaligned W surface on the outer divertor strike point. Very little impact on the plasma was seen. This is rather different from some of the bulk melting experiments and events that have been reported on the ASDEX-Upgrade and C-Mod tokamaks, which in some cases had a catastrophic effect on the main plasma and caused disruptions in subsequent pulses.
- The observed melt on JET is very reproducible pulse by pulse and shallow compared to bulk melting. The damage inflicted during pulse number 87724 at significantly lower base temperature than in subsequent melt discharges is also a clear indication for transient melting. Hence effects of shallow melting with conclusions towards ITER has been achieved

- Most of the melted material is driven out of the high heat flux area. Similar situation can occur depending on the damage locations in ITER/ There are very few droplets ejected and these are small enough to have little effect on the plasma. The physics of W droplets should be machine size independent, whereas screening and resistance to the effects of W radiation improves with machine size.
- While there will probably not be enough thermal stored energy in early ITER plasmas for ELMs to melt the whole strike point area, the JET results are directly relevant to what would happen in the case of an exposed edge. They suggest that provided such an event is detected in ITER and is not repeated too many times such that large droplets accumulate, there would be no significant additional risk of disruption.
- Although the evidence points to the inter-ELM temperature being just below that required for bulk melting, the JET results are still positive even if slight bulk melting had occurred. In this sense the conclusions drawn from the experiment are conservative.
- The inter-ELM temperature falls off more rapidly along the lamella edge than the ELM power load and so post-mortem examination will yield results for a range of conditions with respect to inter-ELM surface temperature.
- The power load on the JET special lamella is substantially lower than expected from both straightforward geometric considerations and PIC code simulations which take into account ion Larmor radius smoothing effects. Although not yet understood, this has potentially positive implications for ITER, which may be less sensitive to exposed edges than had been feared.
- The JET experiment has been used to benchmark the MEMOS code predictions and the code seems able to accurately reproduce the JET melt behaviour when a consistent set of heat flux data are used. This gives confidence in the prediction made for transient melting in ITER.

The physics of melting by transients and melt motion is complex and there are aspects such as the grazing geometry in ITER which could not be matched in the JET experiments. JET also had to pre-heat the W close to the melting point so the thermal stresses on the material are different from those expected in ITER for larger transients and a lower base temperature.

5. SUMMARY AND CONCLUSIONS

A dedicated experiment in support of ITER has been performed in JET to help address the uncertainties associated with trying to predict the impact of ELM-induced transient W melting in ITER. The JET ELMs were of a size relevant to mitigated ELMs in ITER and produced very reproducible W melting and melt motion on a well characterized misaligned edge deliberately engineered into one module of the JET bulk W outer divertor. During a series of 7 consecutive pulses, themselves preceded by several experimental preparatory sessions on JET ~ 150–300μm of W was removed from the exposed edge per pulse (~ 5 – 10μm per ELM). This ELM induced melting produced an enhanced W source, including occasional expulsion of small droplets (80 – 100μm) which do not significantly impact the main plasma.

The melt layer motion appears to be dominated by $j \times B$ forces from thermo electric emission, implying significant current flow during ELMs originating from the hot metal surface. Due to the magnetic geometry, the melted material moves predominantly into the private region out of the main heat flux area and similar behavior would be expected in ITER where material would move away from the main heat-flux affected areas. The physics determining the size of the W droplets should be machine size independent whereas screening and resistance to the effects of W radiation improves with machine size hence allowing for even more stable operation of a larger size machine such as ITER given the same droplet source.

An unexpectedly large mitigation of the heat-flux impinging on the exposed edge was observed in the JET experiment and suggests that under some circumstances at least, such misalignments are less vulnerable to melt damage than had been previously thought. The physics of this mitigation are not yet understood. Larmor-radius smoothing, local transport as well local recycling and particle as well as energy reflection need to be further investigated.

The JET results have demonstrated that W melting by ELMs is consistent with simulations using the MEMOS code which has been used to inform decisions on the choice of W as the material for the first divertor in ITER.

ACKNOWLEDGEMENTS

This work was supported by EURATOM and carried out within the framework of the European Fusion Development Agreement. The views and opinions expressed herein do not necessarily reflect those of the European Commission. The views and opinions expressed herein do not necessarily reflect those of the European Commission ITER Organization. This work was part of the DSOL-25 Joint experiments of the ITPA. This work was also supported by Project GAP205/10/2055 of the Czech Science Foundation.

REFERENCES

[1]. Coenen, J. et al. Nuclear Fusion, **53** (2013), 7, 073043.
[2]. Brezinsek, S. et al. Nuclear Fusion, **53** (2013), 8, 083023.
[3]. Pitts, R. et al. Journal of Nuclear Materials, **415** (2011), 1 SUPPL, –.
[4]. Bazylev, B. et al. Journal of Nuclear Materials, **390–391** (2009), 810–813.
[5]. Pitts, R. et al. Journal of Nuclear Materials, (2013), **438**, S48.
[6]. Coenen et al, J. PSI 2014 – submitted to Journal of Nuclear Materials, (2014).
[7]. Arnoux et al., G. PSI 2014 – submitted to Journal of Nuclear Materials, (2014).
[8]. Coenen, J. W. et al. Nuclear Fusion, **51** (2011), 8, 083008.
[9]. Coenen, J. W. et al. Nuclear Fusion, **51** (2011), 11, 113020.
[10]. Tokar, M. et al. Nuclear Fusion, **52** (2012), 013013.
[11]. Coenen, J. et al. Journal of Nuclear Materials, **438** (2013), S27.
[12]. Krieger, K. et al. Physica Scripta, **T145** (2011), 014067.

[13]. Krieger, K. et al. Journal of Nuclear Materials, **451** (2011), 211.
[14]. Lipschultz, B. et al. Nuclear Fusion, **52** (2012), 12, 123002.
[15]. Garkusha, I. et al. Journal of Nuclear Materials, **390–391** (2009), 814–817.
[16]. Bazylev, B. et al. Fusion Engineering and Design, **75–79** (2005), 407–411.
[17]. Loarte, A. et al. Nuclear Fusion, **54** (2014), 3. Cited By (since 1996)3.
[18]. Sieglin, B. et al. Plasma Physics and Controlled Fusion, **55** (2013), 12, 124039.
[19]. Matthews, G. F. et al. Physica Scripta, **2014** (2014), T159, 014015.
[20]. Bazylev et al., B. PSI 2014 – submitted to Journal of Nuclear Materials, (2014).
[21]. Bazylev, B. et al. Journal of Nuclear Materials, **438** (2013), SUPPL, S237–S340.
[22]. Igitkhanov, Y.; Bazylev, B. and Landman, I. Fusion Science and Technology, **62** (2012), 1, 34–38.
[23]. Bazylev, B. et al. Journal of Nuclear Materials, **417** (2011), 1–3, 655–658.
[24]. Bazylev et al., B. Physica Scripta, **T145** (2011), 014054.
[25]. Bazylev, B. et al. Journal of Nuclear Materials, **415** (2011), 1 SUPPL, S841–S844.
[26]. Bazylev, B. et al. Fusion Engineering and Design, **84** (2009), 2–6, 441–445.
[27]. Bazylev, B. et al. Fusion Engineering and Design, **83** (2008), 7–9, 1077–1081.
[28]. Bazylev, B. et al. Journal of Nuclear Materials, **363–365** (2007), 1011–1015.
[29]. Arnoux, G. et al. Physica Scripta, **2014** (2014), T159, 014009.
[30]. Mertens, P. et al. Physica Scripta, **2009** (2009), T138, 014032.
[31]. Dejarnac et al., R. Accepted for Publication in Nuclear Fusion, (2014).
[32]. Dejarnac, R. et al. Journal of Nuclear Materials, **415** (2011), 1, Supplement, S977–S980.
[33]. Arnoux, G. et al. Review of Scientific Instruments, **83** (2012), 10, 10D727.
[34]. Balboa, I. et al. Review of Scientific Instruments, **83** (2012), 10, 10D530.
[35]. Eich, T. g. et al. Journal of Nuclear Materials, **415** (2011), 1 SUPPL, S856–S859.
[36]. van Rooij, G. et al. Journal of Nuclear Materials, **438** (2013), S42.
[37]. Tanabe, T. Atomic and Plasma-Material Interaction Data for Fusion, **5** (1994), 129.
[38]. STF-8300M – https://www.sbig.com/products/cameras/stf-series/stf/stf-8300m/.
[39]. Coffey, I. H. and Contributors, R. B. J. E. Review of Scientific Instruments, **75** (2004), 10, 3737–3739.
[40]. Wolf, R. C. et al. JET IOP Preprint, (1995). JET-P(95)34.
[41]. Puetterich, T. et al. Plasma Physics and Controlled Fusion, **55** (2013), 12, 124036.
[42]. Puetterich, T. et al. Plasma Physics and Controlled Fusion, **50** (2008), 8, 085016.
[43]. Corr, Y., et al. PSI 2014 – submitted to Journal of Nuclear Materials, (2014), P3-086.
[44]. Mertens, P. et al. Journal of Nuclear Materials, **415** (2011), s943–s947.
[45]. Dejarnac, R. et al. Journal of Nuclear Materials, **390–391** (2009), 1, 818–821.
[46]. Rooij et al., G. PSI 2014 – submitted to Journal of Nuclear Materials, (2014), P3-064.
[47]. Zielinski, J. et al. Applied Physics Letters, **104** (2014), 12. Cited By (since 1996)0.

	n_e $[m^{-3}]$	$T_e = T_i$ [eV]	ρ_L [mm]	$q_{\|\|}$ [GW/m2]
Scenario 1 (S1)	7.1019	500	1.8	7.10
Scenario 2 (S2)	4.1019	300	1.4	1.90
Scenario 3 (S3)	2.1019	100	0.8	0.18

Table 1: Scenarios used in estimating the influence of Lamor-radius smoothing on the heat flux impact of ELMs. ([31]).

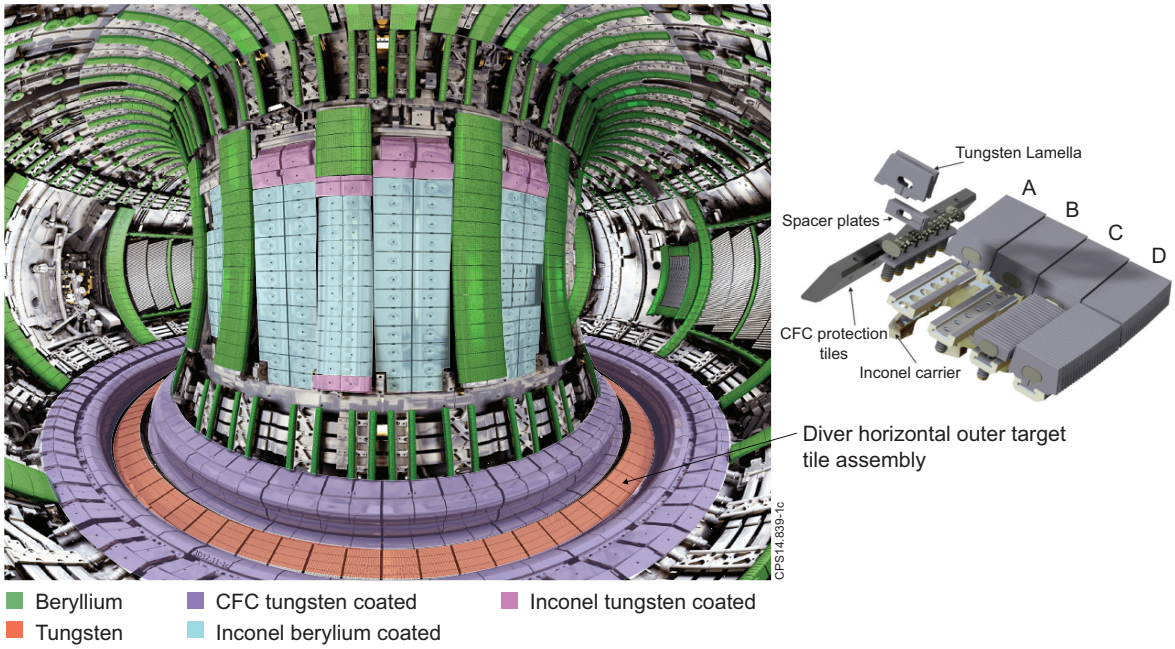

Figure 1: JET ITER-like(ILW) wall PFC distribution and tile assembly of the horizontal, outer divertor target on which melt experiments were performed. This Figure was originally published in [29].

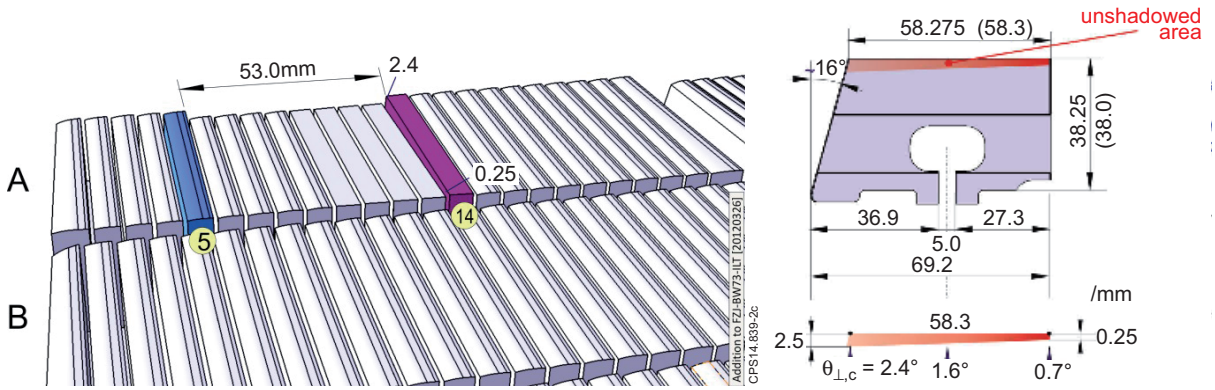

Figure 2: Assembly of the modified stack and design of the special lamella: (a) Schematic view of the lamella assembly in the modified Stack A, (b) Design and dimensions of the special lamella with predicted exposed side (in red).

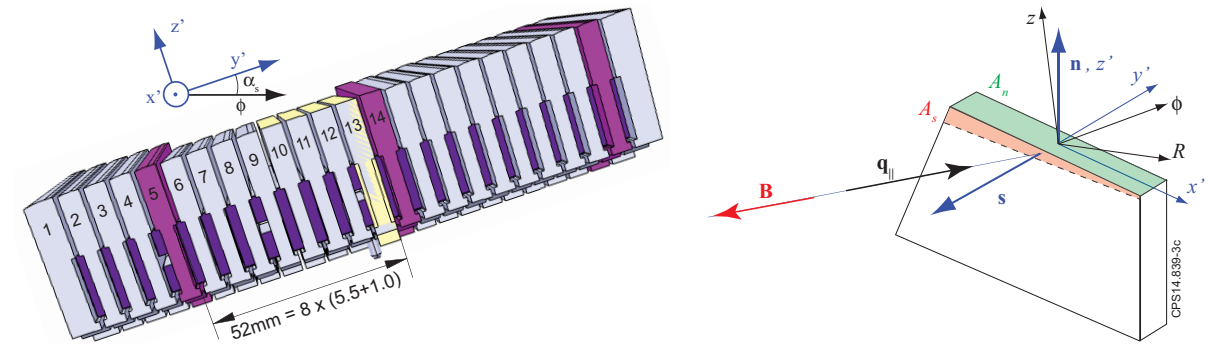

Figure 3: Definitions of the frames of reference in local coordinates and machine coordinates (cylindrical): (a) Schematic view from the front (LFS) of the lamellas assembly in the modified Stack A (b) Schematic view of the local geometry near the special lamella.

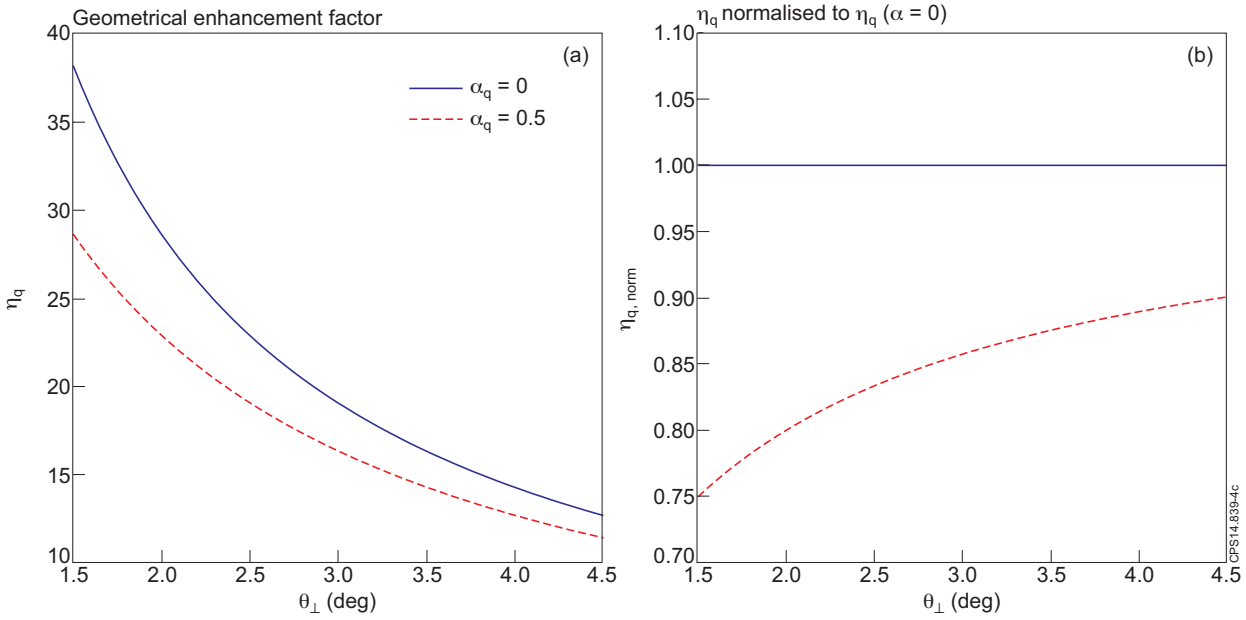

Figure 4: (a) Geometrical flux enhancement factor, η_q , as a function of typical values of $\theta_\perp$ for two toroidal inclination of the stack: α_s = 0 and α_s = 0.5°. (b) Ratio η_q/η_q (α_s = 0) as a function of $\theta_\perp$.

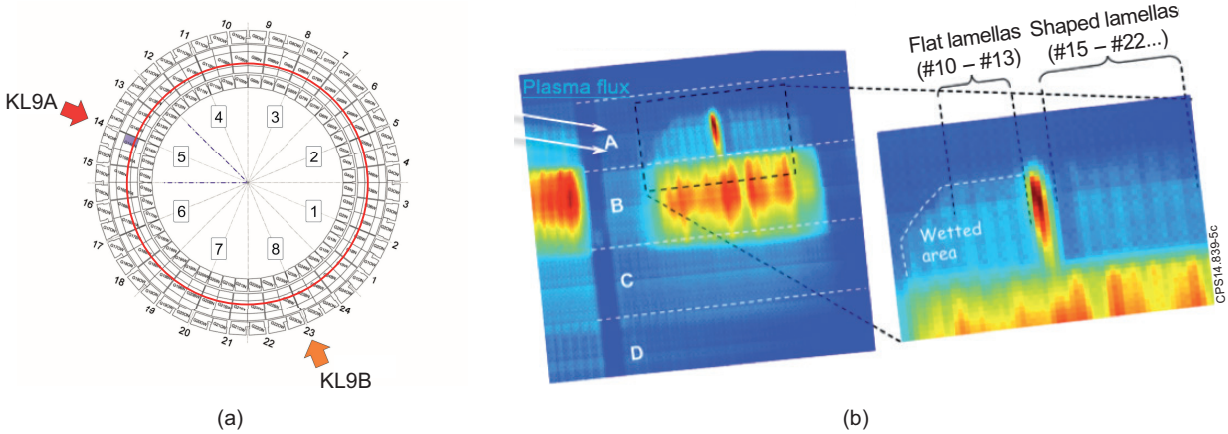

Figure 5: (a) IR cameras positions (KL9A/KL9B) and Stack A/ strike line (red-line) and (b) IR response during exposure of the special lamella in L-mode (KL9A).

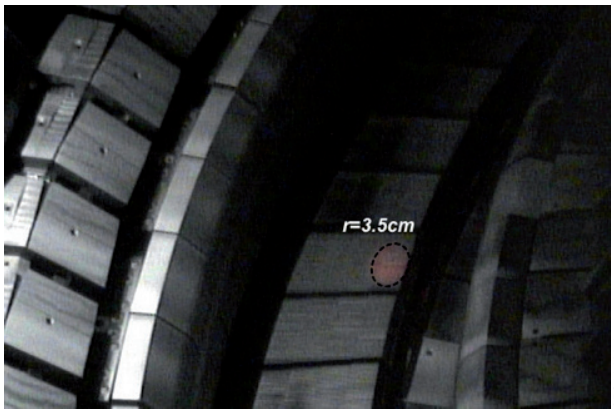

Figure 6: Backlit observation volume for the local W spectroscopy.

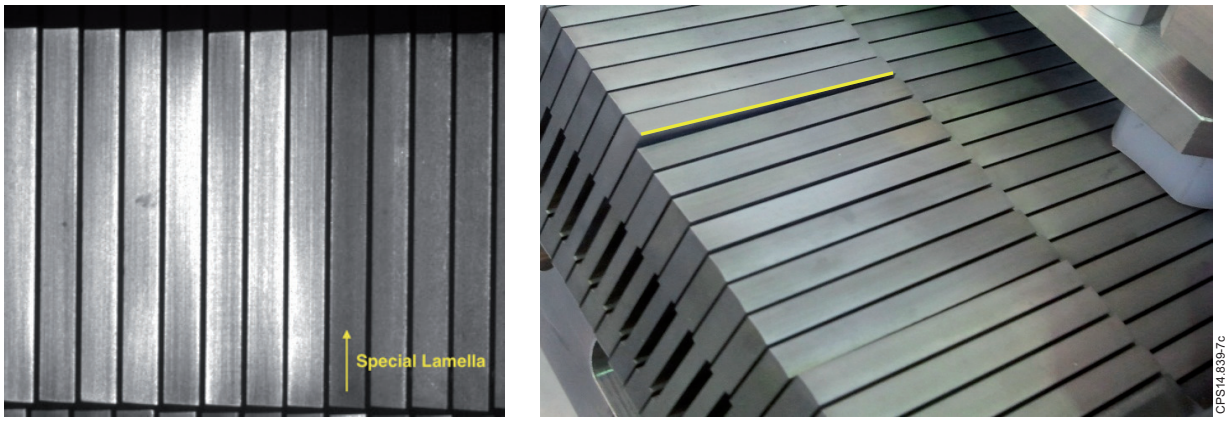

Figure 7: Images of Stack A before the experiments: (a) Top view from high resolution intershot observation, (b) Stack A before installation - yellow bar indicates leading edge.

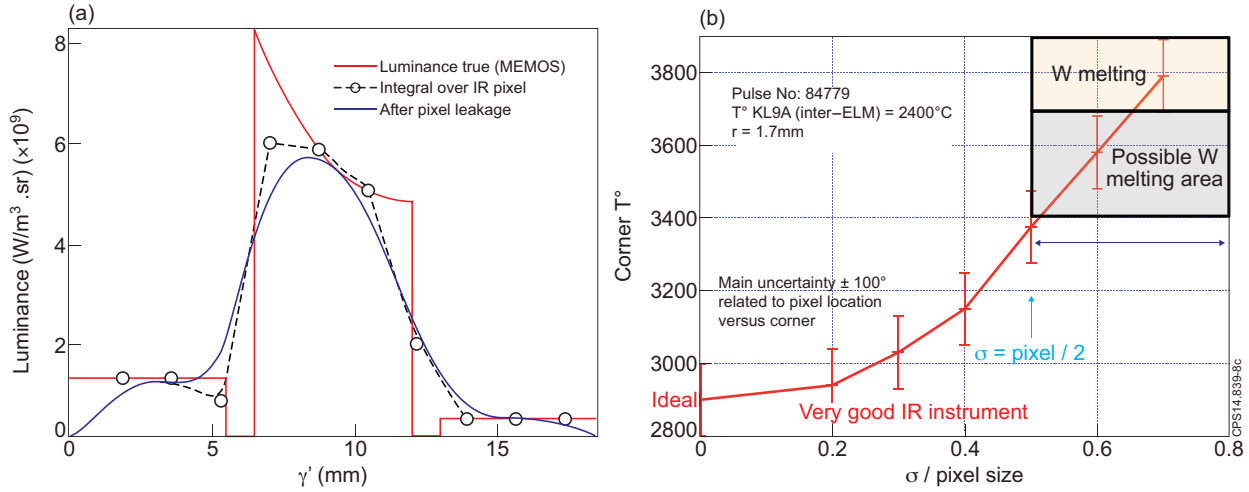

Figure 8: Detrimental effects on temperature determination due to IR observation geometry and IR-camera resolution (compare also [43]): (a) Luminance vs measurement, (b) Effect of pixel leakage on temperature determination.

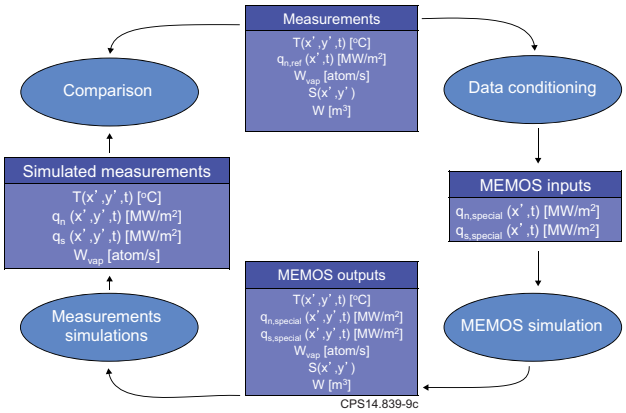

Figure 9: Evaluating thermal data.

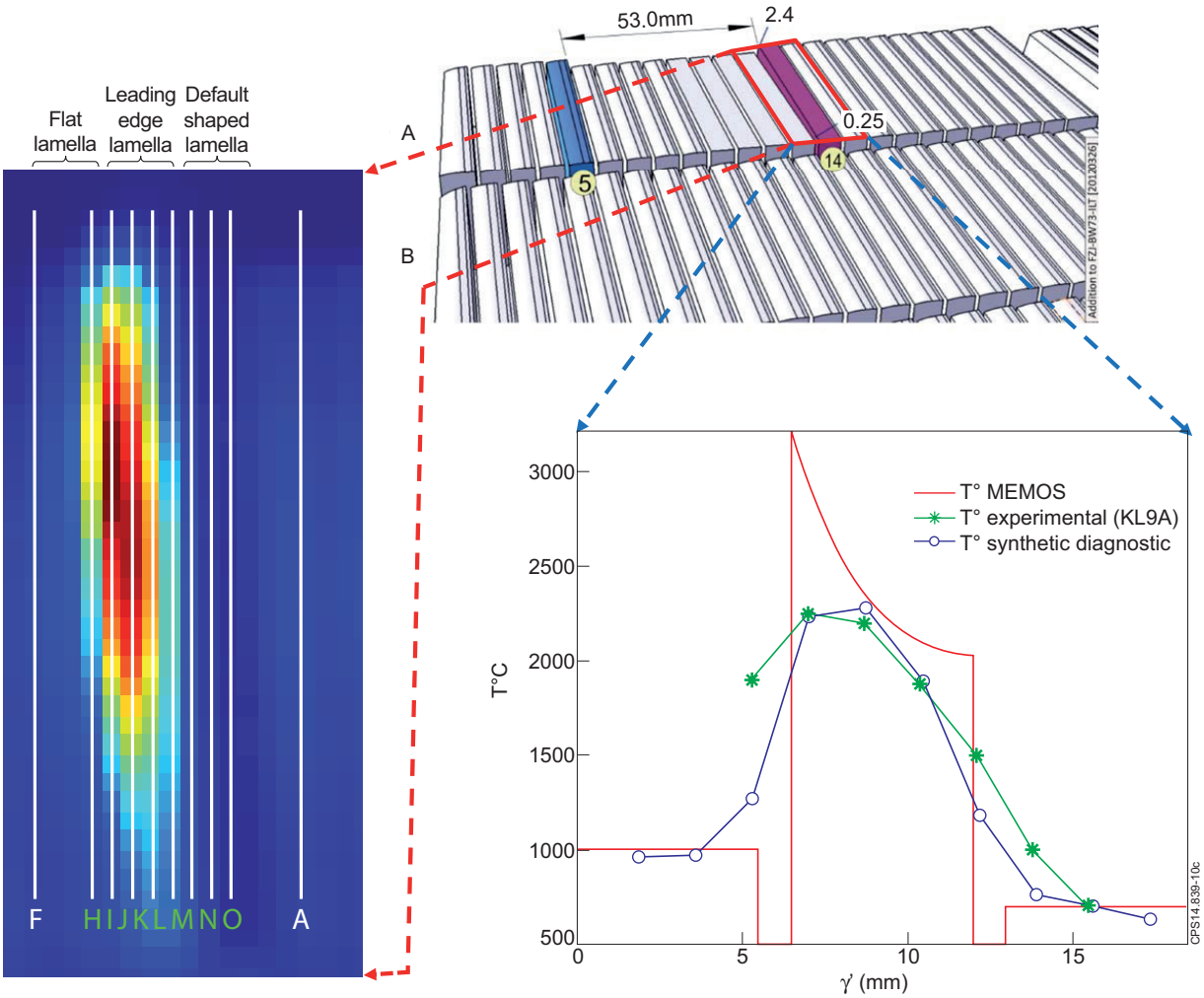

Figure 10: Comparison of measured IR data – Modeled temperature response (Red) and synthetic diagnostic (Blue) [43].

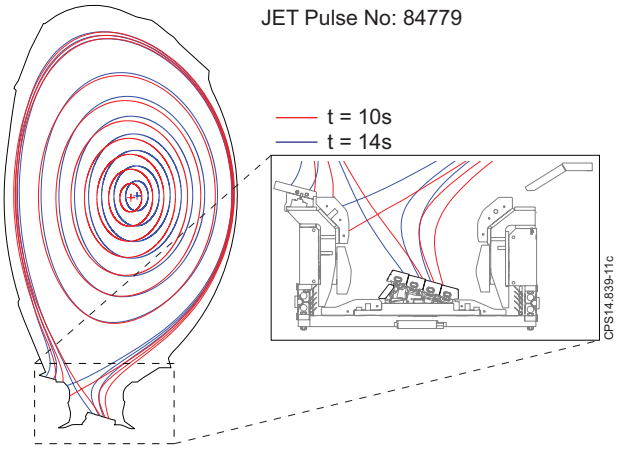

Figure 11: Equilibrium reconstruction (EFIT) at two times during pulse number 84779. At t = 10.0s (red) the outer strike point (OSP) is on stack B and at t = 14.0s the OSP is on stack A.

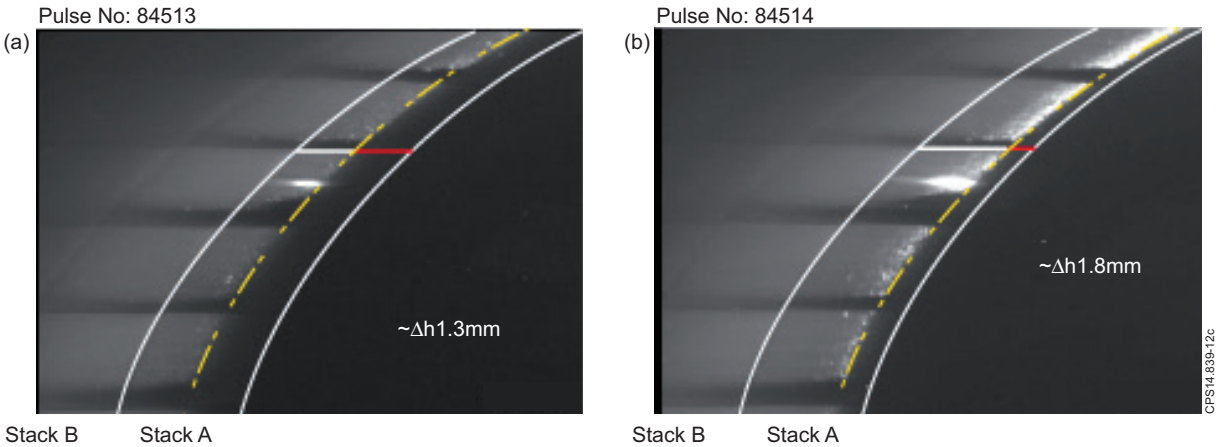

Figure 12: L-Mode exposure of the modified lamella – Strike line positioning.

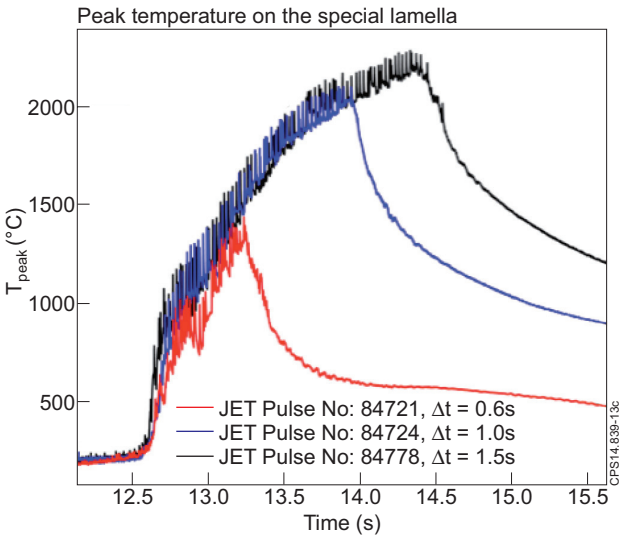

Figure 13: Temperature evolution on the special lamella for three different durations. (Temperature given as measured without correction).

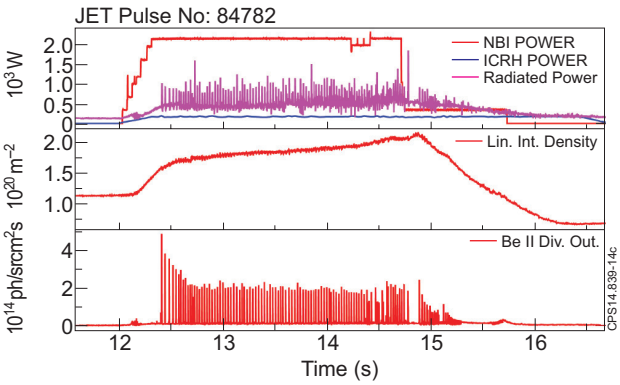

Figure 14: Parameters of pulse number 847782 including Be II Divertor emissions used to distinguish ELMs. Injected Power by Neutral Beam (NBI) and RF-Heating (ICRH). The pulses were performed using deuterium plasma.

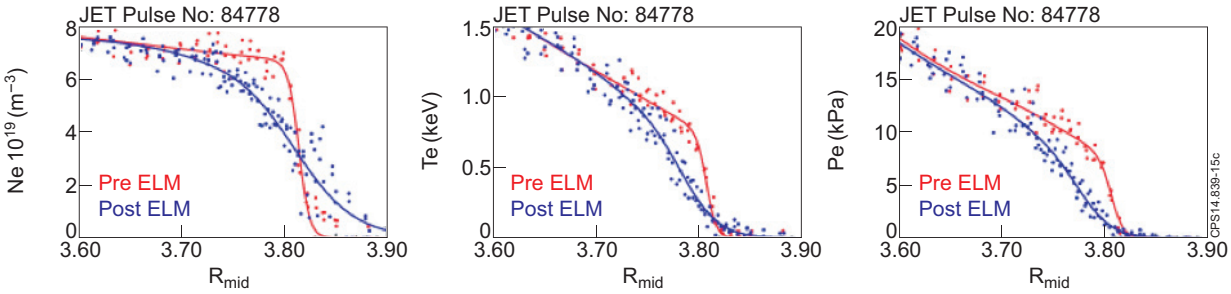

Figure 15: Pedestal parameters during pulse number 84778 measured from thomson scattering.

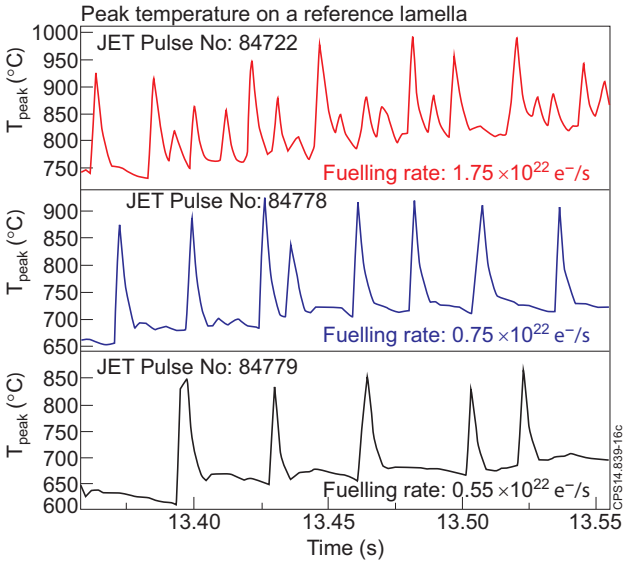

Figure 16: ELM behavior for a plasma at Ip = 3MA, and a fuelling rate of 1.75 × 10^{22}el/s (top), 0.75 × 10^{22}el/s (middle) and 0.75 × 10^{22}el/s (bottom). Data given for a standard shaped lamella.

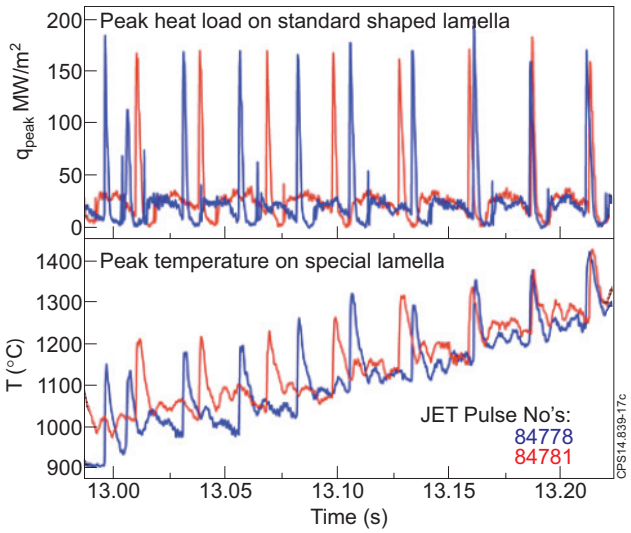

Figure 17: ELM Temperature measurement for two pulses used in the experiment. Both shown for the reference and the special laemalla.

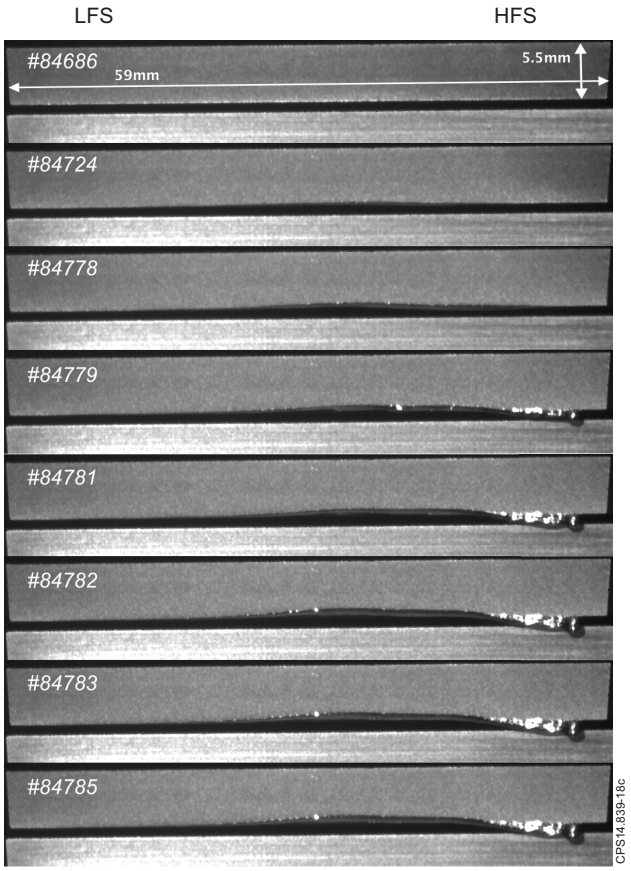

Figure 18: High resolution camera images of the special lamella taken after each pulse in the sequence of melt pulses. Damage after each melt exposure including pre-melt status (pulse number 84686) and after pulse number 84785).

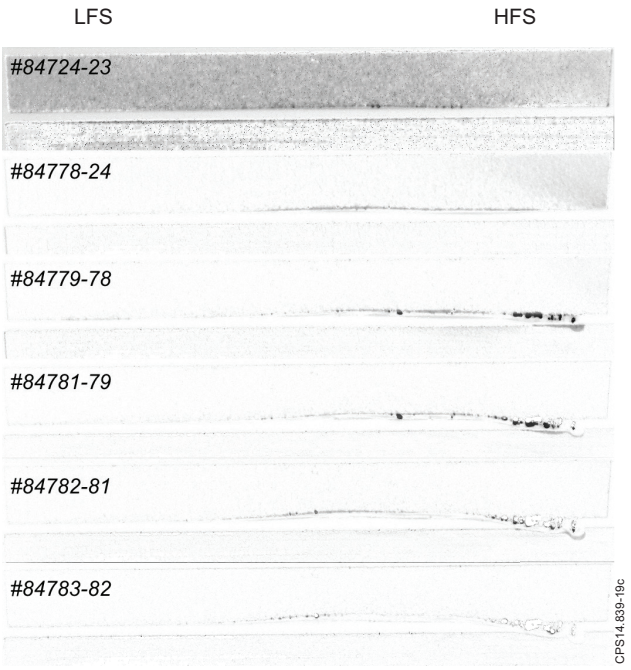

Figure 19: High resolution camera images of the special lamella taken after each pulse in the sequence of melt pulses. Differential damage images – illustrating damage evolution.

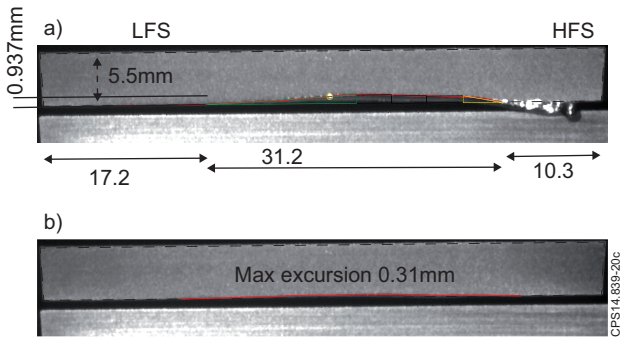

Figure 20: Geometrical estimation of material moved during all melt pulses a) after all exposures, b) after pulse number 84724 only.

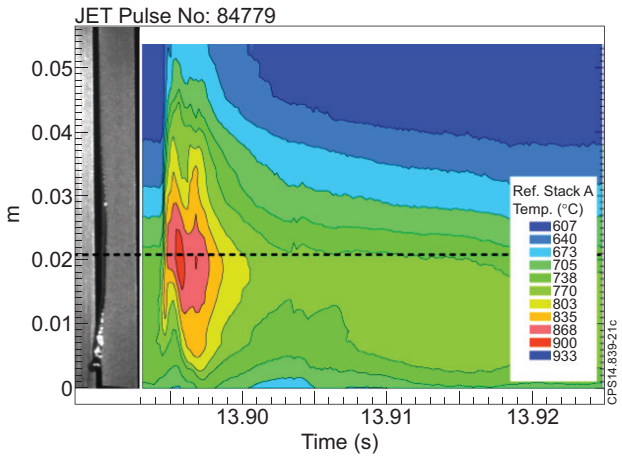

Figure 21: Thermal footprint of the flat reference lamella compared to inflicted surfaces damage in special lamella.

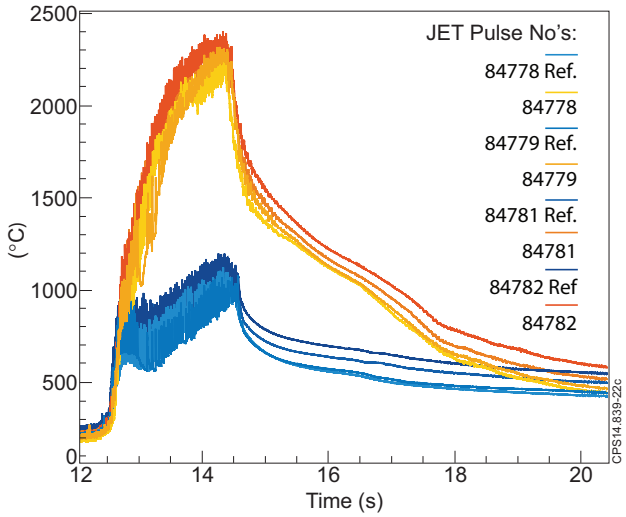

Figure 22: As-measured peak temperature values on both a flat reference as well as the special lamella for each of the four 1.5s long melt exposure pulses where most of the melting was observed (pulse numbers 84778-82).

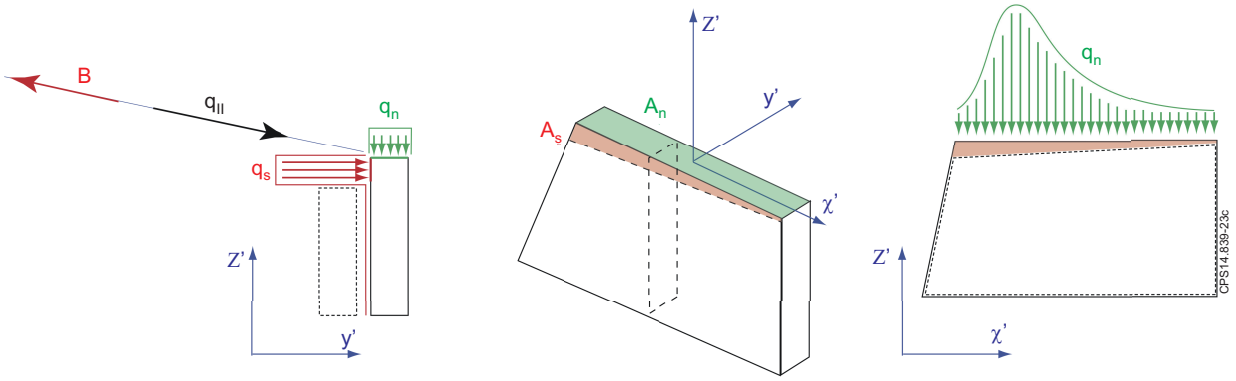

Figure 23: Schematic picture of geometry and impinging heat fluxes.

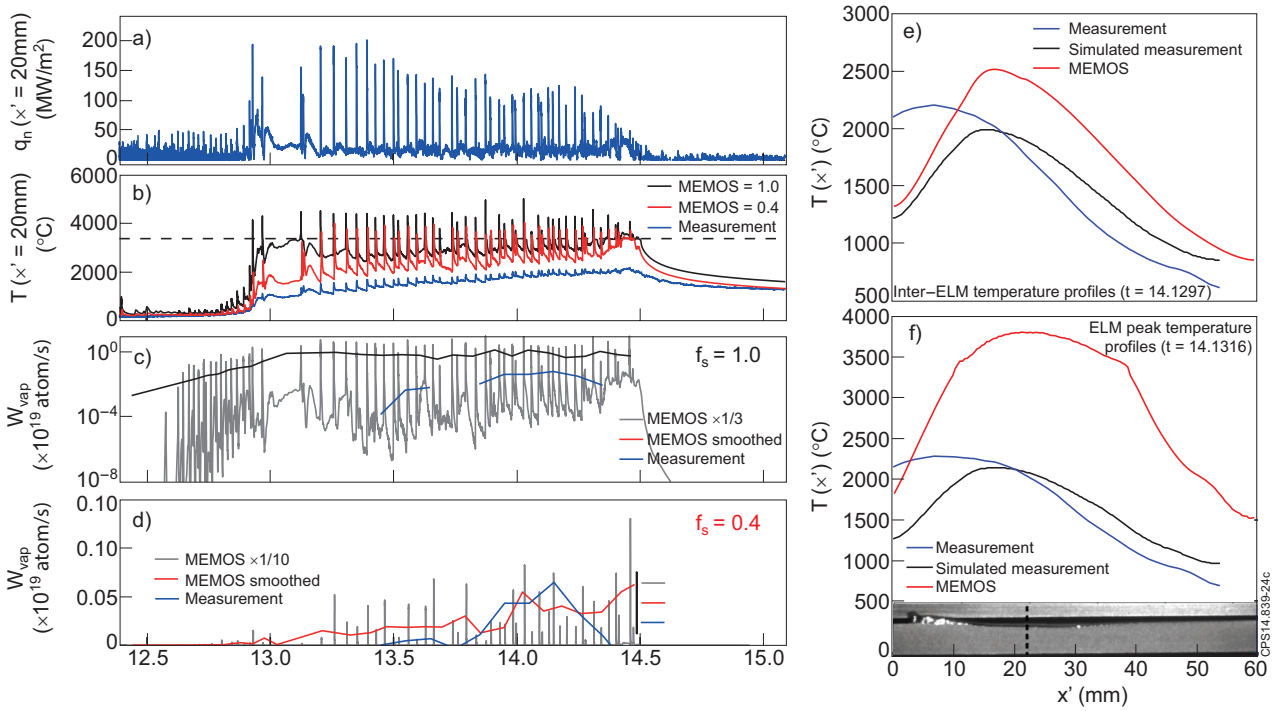

Figure 24: Comparison of data for pulse number 84779 – time evolution of the measured peak heat flux on the flat reference lamella, $q_{n,peak}$ (t) (a), the measured and simulated (MEMOS) peak temperature of the melted lamella, T_{peak} (t) (b) and the measured and simulated W vaporisation rate for two different heat flux reduction factor, f_s = 1 (c) and f_s = 0.4 (d). In (b) the simulated temperatures are shown for both f_s = 1 (black) and f_s = 0.4 (red). The original simulated W_{vap} in (c) and (d) is time averaged over 100ms to simulate the measurement (exposure time of the spectrometer), leading to the black (c) and red (d) traces. (e) and (f) temperature profiles before and at the peak of an ELM respectively, measured (blue), simulated by MEMOS (red) and simulated measurement from MEMOS (black). In (f) a zoomed picture of the melted lamella is inserted and the dashed line indicate the deepest, reference melt thickness.

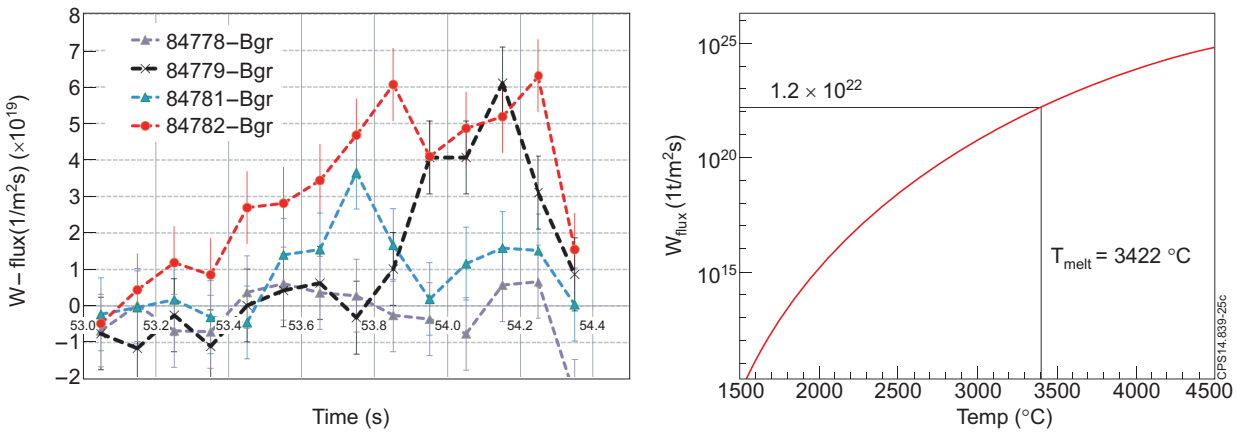

Figure 25: W Evaporation as measured (a) and from theory (b).

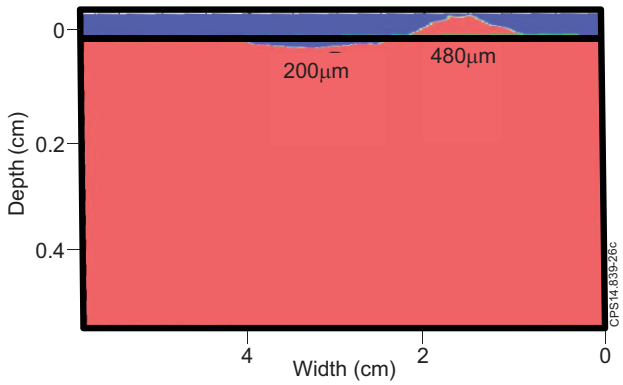

Figure 26: Melt Layer Modeling - Material redistribution based on MEMOS calculation is shown. Material moved after 1 melt pulse (Input data based on pulse number 84779).

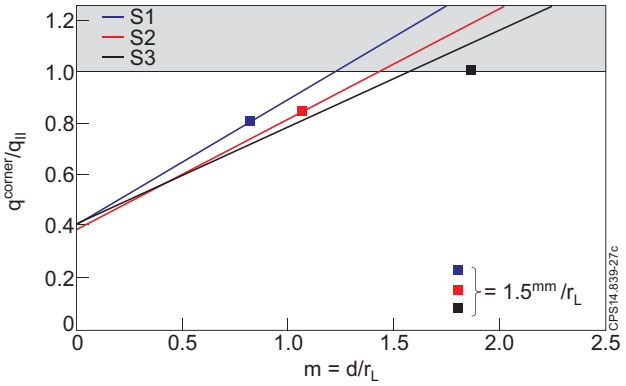

Figure 27: Scaling law for the power flux normalized to $q_{//}$ falling on the corner of the special lamella for different ELM scenarios as a function of the misalignment normalized to the Larmor radius. S1, S2, S3 are assumptions on the ELM parameters during the experiments [31].

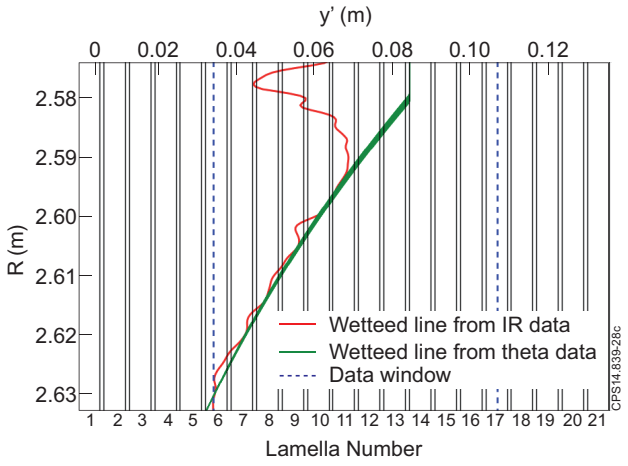

Figure 28: Wetted Area from geometrical assumptions vs measured IR Footprint. The green line depicts the geometrical border of the shadow given from the field line geometry the red line is the measured IR footprint.

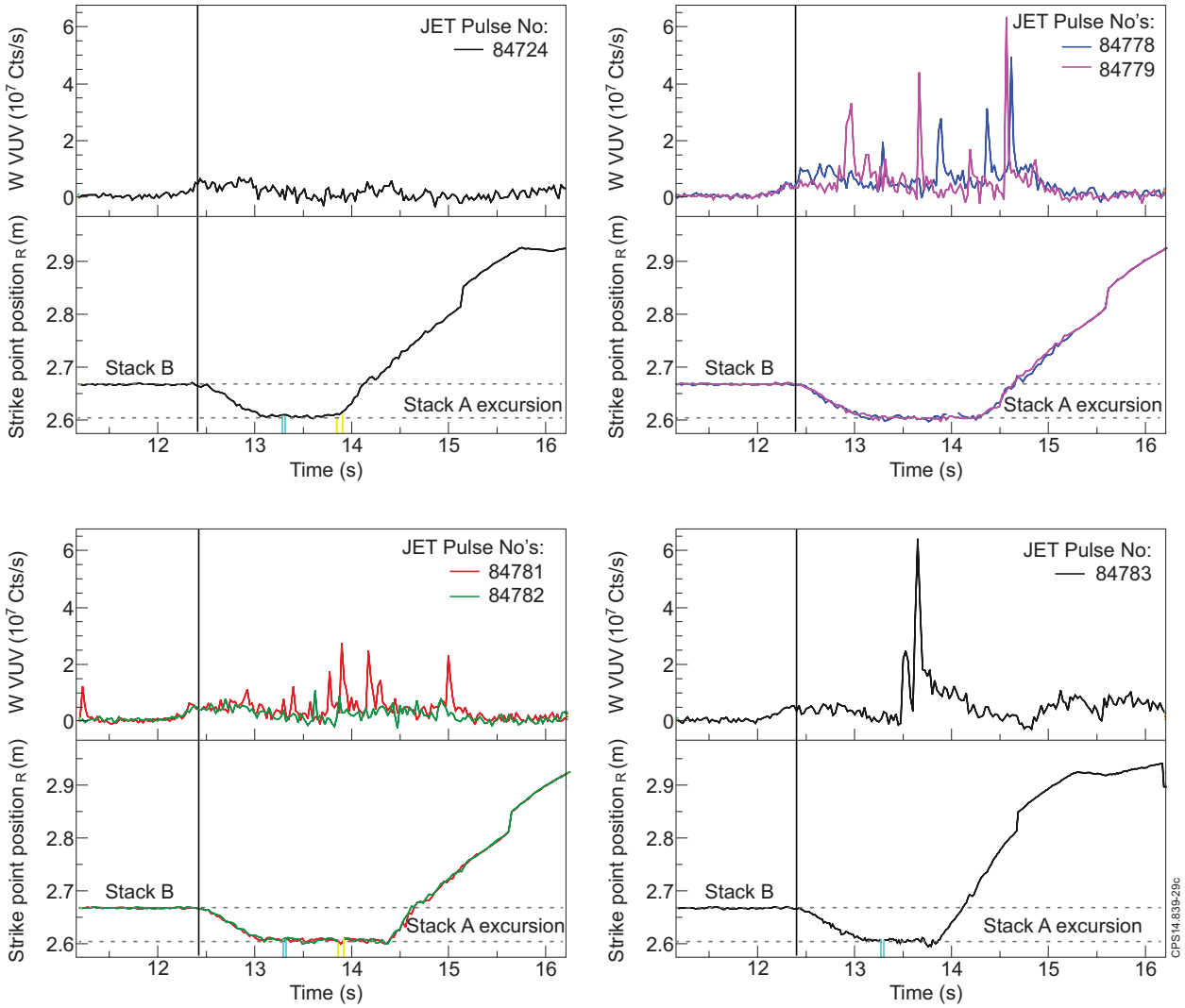

Figure 29: VUV W Signals for individual melt exposures as well as the respective Strike-Point position.

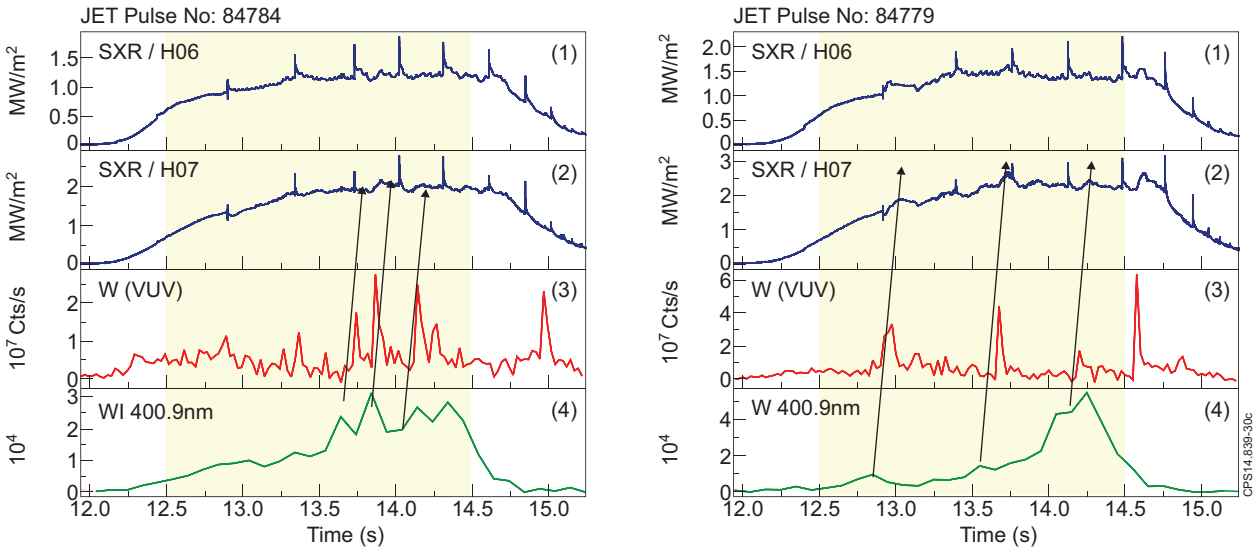

Figure 30: The impact of the local W source (green) on core plasma signals such as VUV W emissions (red) and soft-xray emissions (blue).

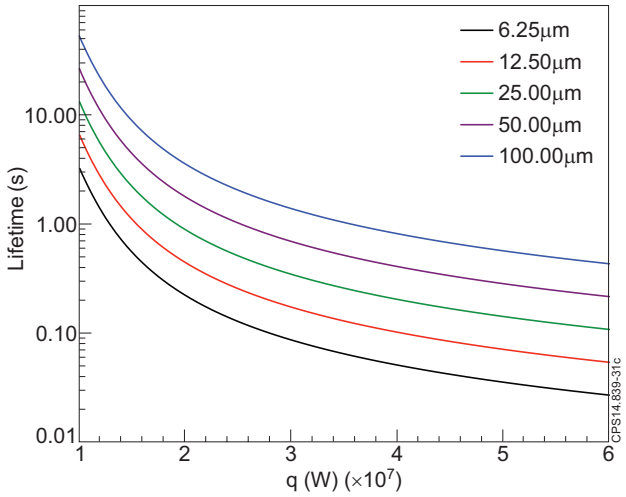

Figure 31: W Droplet Lifetime with respect to impinging parallel heat fluxes.

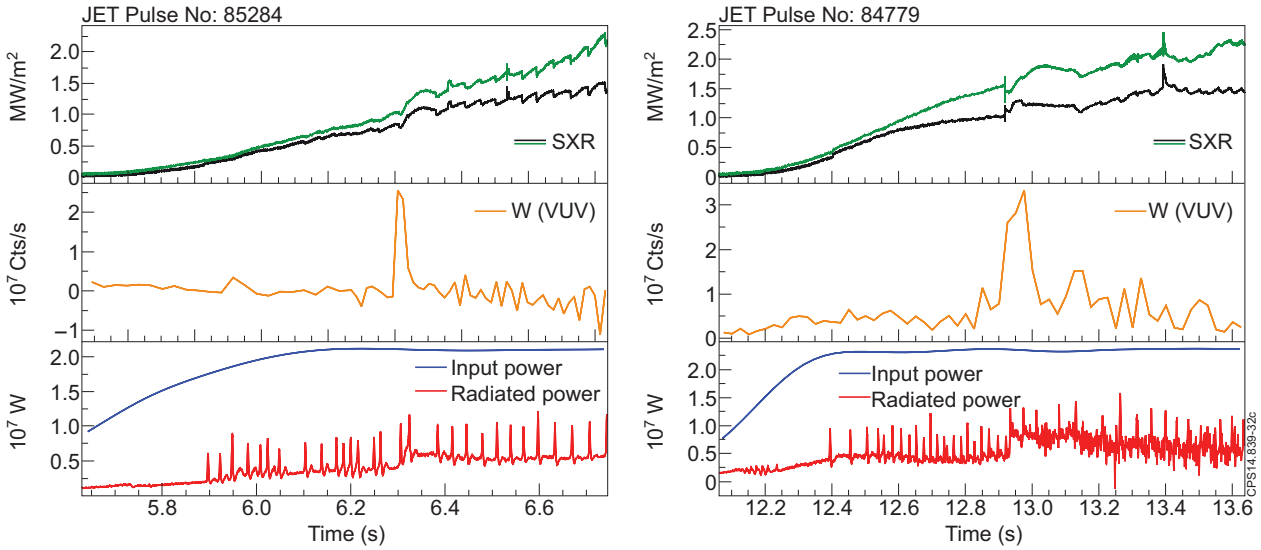

Figure 32: Transient W sources and their impact on plasma radiation losses: LBO (left), Melt Droplet (right).